STELLAR TRACKING ATTITUDE REFERENCE SYSTEM

System Application Study

Author: B. Klestadt
Hughes Aircraft Company
Space and Communications Group
1950 E. Imperial Highway
El Segundo, California
90009

Final Report

September 1974
Contract No. 5-21846

Prepared for
GODDARD SPACE FLIGHT CENTER
Greenbelt, Maryland 20771

FOREWORD

The study described in this report was performed by the Guidance and Control Systems Laboratory, Technology Division, Space and Communications Group, Hughes Aircraft Company, El Segundo, California. The work was accomplished under NASA Contract NAS 5-21846, with Mr. H. Paul Scherer, Stabilization and Control Branch, Spacecraft Technology Division, Engineering Directorate, Goddard Space Flight Center, Greenbelt, Maryland as Technical Officer. The principal members of the project team were as follows:

B. Klestadt, Project Manager
F. H. Minami
R. J. Roy
J. Schrier
R. W. Wood

Preface

This final report documents the detailed results of a system application study, involving the use of the Hughes Stellar Tracking Attitude Reference System (STARS) as the attitude reference for precision pointing (with .001 degree accuracy) of an EOS spacecraft. The STARS accomplishes precision earth pointing by utilizing a single, clustered star tracker assembly mounted on a non-orthogonal, two gimbal mechanism, driven so as to unwind satellite orbital and orbit precession rates.

The fundamental objective of the system application study was to explore, by means of realistic preliminary design, analysis, and simulation, the limitations placed upon STARS performance in a typical low altitude, inclined orbit earth observation mission by the non-ideal characteristics of the system hardware and spacecraft behavior. A basic ground rule of the study was that gyros were not to be used to provide short period stabilization.

The overall conclusion reached in this study is that a relatively straightforward precision pointing system design, utilizing STARS on an EOS type spacecraft, and considering the characteristics of real sensing and control components, can achieve the desired 0.001 degree pointing capability. It was found that the lower limit on long term pointing precision was determined primarily by the accuracy obtainable from the star trackers. Short term pointing precision (jitter) was easily reduced to below 0.2 arcseconds by proper control system design, and both good jitter stability and excellent transient response characteristics were obtained without the use of gyros. Since all analyses and simulations so far have shown STARS to be capable of the desired pointing precision and stability, the next step in bringing STARS up to the level of a flight qualified system is the development of an engineering model and it is therefore recommended that this be undertaken next.

TABLE OF CONTENTS

ILLUSTRATIONS

ILLUSTRATIONS

(continued)

TABLES

1. Introduction

The requirements of various projected scientific, commercial, and defense oriented satellite missions indicate a strong need for a straightforward, conceptually simple, mechanically and electronically uncomplicated, and highly reliable attitude reference and precision pointing system, which has the potential of achieving and the possibility of eventually exceeding 0.001 degree pointing capability. In response to this need, Hughes Aircraft Company has evolved the STARS (Stellar Tracking Attitude Reference System) concept which avoids many of the problems associated with the precision pointing schemes by the use of a compact multistar tracker and a simple, unconventional two-gimbal assembly. The advantages of this approach are as follows:

1) The stellar reference is a single, clustered star tracker assembly on a single gimbal mount, thus providing a uniform thermal environment for its components, minimum distortion, and involving minimum interaction with other spacecraft components.

2) The STARS concept is not dependent upon high precision gyros, with their attendant reliability and cost disadvantages.

3) The star tracker concept provides a high level of redundancy in its basic design, being able to track more than the minimum required number of stars most of the time. In addition, it provides gradual degradation of performance in case of failure of one or more individual trackers.

4) The star tracker design and the particular scanning technique used avoid the usual requirements for critical alignment of the scanning device to the boresight axis.

5) The STARS concept operates with essentially constant rates about both gimbal axes, thereby avoiding many of the more significant sources of angular error normally associated with gimbal systems and their drives.

6) The STARS concept minimizes the amount of computational capability required of the on-board computer.

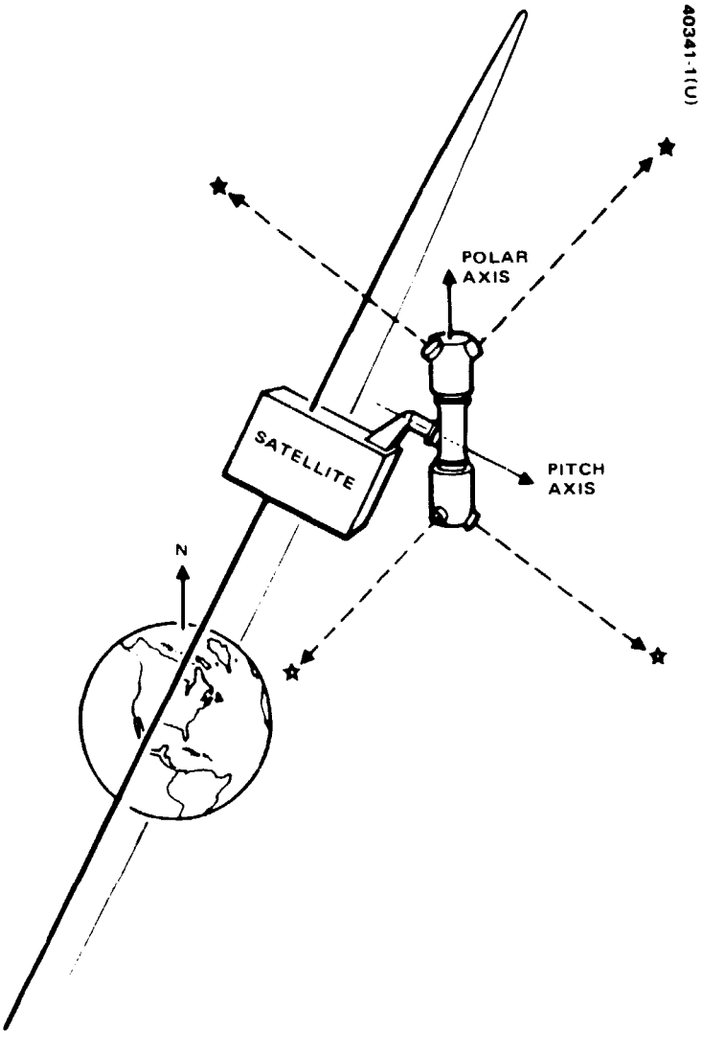

FIGURE 1-1. STARS – A GYROLESS INERTIAL PLATFORM

7) The STARS concept can operate without the conventionally required on-board star catalog since the locations of only eight preselected stars are required.

This concept was investigated in NASA funded feasibility study (contract - NAS 5-21508) which ended in June 1971. The design configuration, developed in the feasibility study, utilized a clustered set of eight star trackers mounted on the inner gimbal of a nonorthogonal two-axis gimbal system. As illustrated diagrammatically in Figure 1-1, the inner gimbal is held essentially parallel to the earth's polar axis, while the outer gimbal is parallel to the satellite pitch axis. Under ideal conditions, the satellite may rotate about its pitch axis while keeping the yaw axis pointed precisely vertical, and the star trackers continue to point at their assigned stars while the orbit precesses about the polar axis. The star trackers are arranged and their signals processed so that two are tracking stars at any one time regardless of earth and satellite body occultation directions. Physical motion of the star trackers in inertial space to permit the tracking function is accomplished by controlling vehicle attitude. Precision pointing of the satellite vertical is achieved by commanding the proper pitch and polar axis gimbal angles, based on ground-determined and regularly updated ephemeris data. An on-board digital computer keeps track of local satellite time, calculates and sets proper gimbal angles, and performs the attitude control signal processing and command functions to enable star tracking as required.

This one year study showed that STARS appears to be a feasible attitude reference system and that no theoretical obstacles exist to a practical implementation. Systems analysis showed that a set of eight stars could indeed be found that would provide a continuous attitude reference for any arbitrary orbit. A straightforward attitude acquisition procedure was developed, and the on-board computational requirements were established. A conceptual design and layout of a suitable gimbal system for the star trackers was developed and the availability of the required components was established. Servo analysis and simulation of the gimbal positioning systems showed that precise positioning at the required position accuracies and rates is theoretically feasible. In addition, assembly and test methods for the STARS gimbal system were explored as an essential part of an overall feasibility study.

A detailed analysis and preliminary design of a star tracker system was performed in the feasibility study. This involved a system analysis of the proposed tracker system including optics, signal processing, and sunshade design. A mechanical design study resulted in a detailed preliminary mechanical layout of a tracker cluster and verification that the design concept was feasible. In addition a detailed error analysis of the total system, based on anticipated thermal and structural characteristics, showed that the STARS mechanism is inherently suitable for high precision attitude reference purposes.

An area excluded from consideration in the feasibility study was the precision pointing capability of a real spacecraft employing STARS for sensing, since such a study is spacecraft configuration dependent. A preliminary, linearized analysis for a typical spacecraft, performed since the completion of the feasibility study, has indicated however that under idealized sensing and torquing conditions, with pure angular rate feedback available, precision vertical pointing to 0.001 degree is practical. The questions that were not answered at that time, and that required further detailed study, concerned the limitations placed on precision pointing by realistic star sensor characteristics, signal processing requirements, control system bandwidth limitations due to sensor noise, and the requirement to generate attitude rate damping information from star sensor signals rather than a built-in gyro. These are the principal questions that were addressed by this system application study.

The study can be divided essentially into three parts: star tracker investigations, attitude control system design, and performance analysis and simulation. Each of these areas is discussed in turn on the following pages.

2. Star Tracker Performance

In order to develop more confidence in the ability of the STARS tracker to achieve the required performance in the postulated environment, the tracker noise model developed during the feasibility study was re-examined. Concurrently, to provide improved insight into photomultiplier noise characteristics obtained experimentally on another program, and to confirm the analytical approach, additional tests were performed on three photomultiplier tubes. The analysis and the experimental results are discussed below.

2.1 Analysis

The star detection process basically consists of setting a threshold level and defining voltages below that level "noise" and voltages above that level as "signal". The determination of the appropriate threshold level setting requires a statistical evaluation of the probability of a noise pulse being greater than this level (false alarm) and a signal + noise pulse being smaller than this level (missed pulse). This analysis is based on the assumption that a false alarm is equivalent to a missed pulse in respect to the perturbation it causes to the system's tracking loop.

The STARS star tracker uses photomultiplier tubes as optical detectors. The model that best describes the pulse amplitude distribution of the photomultiplier tube's noise output has been the principal subject of this analysis. It is this model that permits a determination of where to set the detection threshold and prediction of the false alarm and missed pulse rates for this threshold. In earlier analyses, gaussian statistics were used to describe both the signal and noise characteristics of the PMT output. Experience on the Space Precision Attitude Control System (SPACS) star sensor program found that this assumption yielded extremely optimistic results in comparison to laboratory measured performance.

The noise output of a PMT is primarily a result of PMT leakage current, star background irradiance, and illumination from off-axis bright sources such as sun, earth or moon being reflected and scattered by the sun shade into the field of view. Of these, the reflected and scattered solar illumination was considered to be the dominant performance limiting noise source as discussed in the STARS final report.

In addition to these sources of noise; space radiation, in particular high energy galactic particles, may contribute to the PMT output noise.

A study that was performed to explain the discrepancy between the measured and expected false alarm rates on the SPACS program found that the amplitude of the PMT output noise pulses exhibited an exponential distribution rather than gaussian. This distribution results in much higher false alarm rates as will be shown.

The present analysis includes an examination of the pulse amplitude distribution of three representative photomultiplier tubes operated at the conditions of background illumination and electrical bandwidth anticipated for the STARS sensor.

The solar irradiance that is scattered and reflected from the sun shade will result in an average (d.c.) output I_B at the PMT anode. This current can be related to an equivalent signal irradiance at the entrance aperture of the optics by

$$H_B = \frac{I_B}{R\,G\,A_{eff}}$$

where R = Photocathode Responsivity

G = Photomultiplier Gain

A_{eff} = Effective Optical Aperture

The variation of background noise pulse amplitudes is generally described by a gaussian distribution for which the 1σ standard deviation or rms noise is given by

$$i_n(1\sigma) = \sqrt{2e \frac{\delta}{\delta-1} A_{eff} R H_B G^2 \Delta f \text{ (amp)}}$$

where

δ = average gain of an individual dynode

G = multiplier overall gain

Δf = noise equivalent bandwidth

The effective signal irradiance equivalent of this noise current is given by

$$\delta = \frac{i_n}{A_{eff} RG} \quad (\text{watt cm}^{-2})$$

The baseline design parameters, applicable to this analysis, for the STARS sensor are shown in Table 2-1.

TABLE 2-1 BASELINE DESIGN

Photocathode Responsivity, R = .075 amp/watt
Effective Collecting Aperture, A_{eff} = 6.4 cm^2
Noise Equivalent Bandwidth, Δf = 350 hz
Gain of a single dynode, δ = 2.5
Background Irradiance, $H_B = 1.1 \times 10^{-13}$ w/cm^2
Minimum STAR Irradiance, $H_{eff} = 1.1 \times 10^{-13}$ w/cm^2
Pulse Visibility Factor, V_p/Vss = .75

Normalizing irradiance levels and noise currents to the appropriate value of σ provides a simplified means of comparing data taken under different conditions and relating it to the analysis using baseline design parameters.

For the above design parameters, it is found that $\sigma = 6.52 \times 10^{-15}$ watt cm^{-2}. The minimum star therefore can be expressed as

$$H_{eff} \cdot (Vp/Vss) = 12.65\sigma$$

For a gaussian distribution of noise pulse amplitudes, the probability of a pulse exceeding the mean value by an amount T can be described by

$$P_{FA}(T) = \frac{1}{2} - \frac{1}{\sigma\sqrt{2\pi}} \int_0^T \exp\left[-\frac{1}{2}\left(\frac{T}{\sigma}\right)^2\right] dT$$

The gaussian function is generally used to describe noise amplitudes greater than and less than the mean value with equal probability. For the purpose of the analysis of false alarms, only positive amplitudes need by considered, resulting in the $\frac{1}{2}$ factor at the beginning of the above equation.

If the output noise exhibits exponential behavior the distribution of noise amplitudes greater than the mean level can be described by

$$A(T) = \frac{1}{\sigma} \exp\left(-\frac{T}{\sigma}\right)$$

If the assumption is made that the output noise amplitude is greater than the mean level half the time, then the probability of a false alarm as a function of threshold setting above the mean level can be expressed by

$$P_{fa}(T) = \frac{1}{2} - \frac{1}{2\sigma} \int_o^T \exp\left(-\frac{T}{\sigma}\right) dT$$

In the baseline STARS concept, each photomultiplier tube is only active during two 90^o windows. This results in a factor of 2 reduction in the number of effective false alarms.

The probability of missing a pulse is described by the probability that the amplitude of the signal plus noise will be less than the threshold level. One must be certain to include the noise because of the finite probability that the direction of the noise pulse at the time of a signal pulse will subtract from the signal thus increasing its probability of falling below threshold. Since both positive and negative deviations of signal and noise from their mean values must be considered in this portion of the analysis, use of a gaussian distribution is most appropriate. Data obtained on the SPACS system supports use of the gaussian model.

The standard deviation or rms value of the signal + noise is given by

$$i_n' = \sqrt{2e \frac{\delta}{\delta-1} A_{eff} R (H_{eff} + H_B) G^2 \Delta f} \quad \text{(amp)}$$

and the corresponding signal irradiance by

$$\sigma' = \frac{i_n'}{A_{eff} R G} \quad (\text{watt cm}^{-2})$$

For the baseline case in which $H_{eff} = H_B$, $\sigma 1 = \sqrt{2}\,\sigma$

The missed pulse rate is given by

$$MPR = P_{MP} \cdot N$$

where N is the normally expected rate of signal pulses which for a STARS sensor is four per second.

2.2 Experimental Results

A test was set up in which a light source provided a background irradiance at the PMT photocathode. The d.c. or average and the rms noise currents were measured at the output of a 300 hz (3 db) cutoff filter. A threshold was set at the average and the number of frequency of pulses exceeding this value were measured on a counter. This zero threshold (T = 0) level was found to yield a false alarm rate that could be approximately described by

$$FAR \simeq 2P_{fa}\,\Delta f$$

The earlier SPACS study reported a similar finding; however, certain aspects of that study appear to indicate that noise amplitudes below the mean noise level were neglected, which may imply false alarm rates a factor of two greater than those observed in these tests.

The threshold voltage level was increased and data was collected of the frequency of pulses that exceeded each threshold level. These frequencies or count rates were divided by the zero threshold rate to provide the probability of false alarm as a function of threshold and normalized to a value of .5 for the P_{fa} (T = 0).

The three tubes used in this test had the same type of photocathode and were manufactured by the same manufacturer. One tube, 7762E, has a slightly larger photocathode area than the other tubes and was manufactured around nine years ago. A second tube, 13873, was manufactured around four years ago and has been used quite extensively for SPACS engineering tests. The third tube, 19391, is of very recent manufacture and has not been used other than for acceptance type tests.

As seen in Figure 2-1, one tube (13873) behaves in an almost perfect exponential manner and the other two tubes are closer to gaussian. PMT 19391 shows a tendency toward exponential behavior for large amplitude pulses.

The nature of the measurement techniques used to obtain the above data necessitated using data taken over extended periods, many days in some cases. This caused some concern over the accuracy of applying the data to short time intervals. A solution to this shortcoming was found to be through the use of a multichannel analyzer that samples noise and counts the distribution of samples

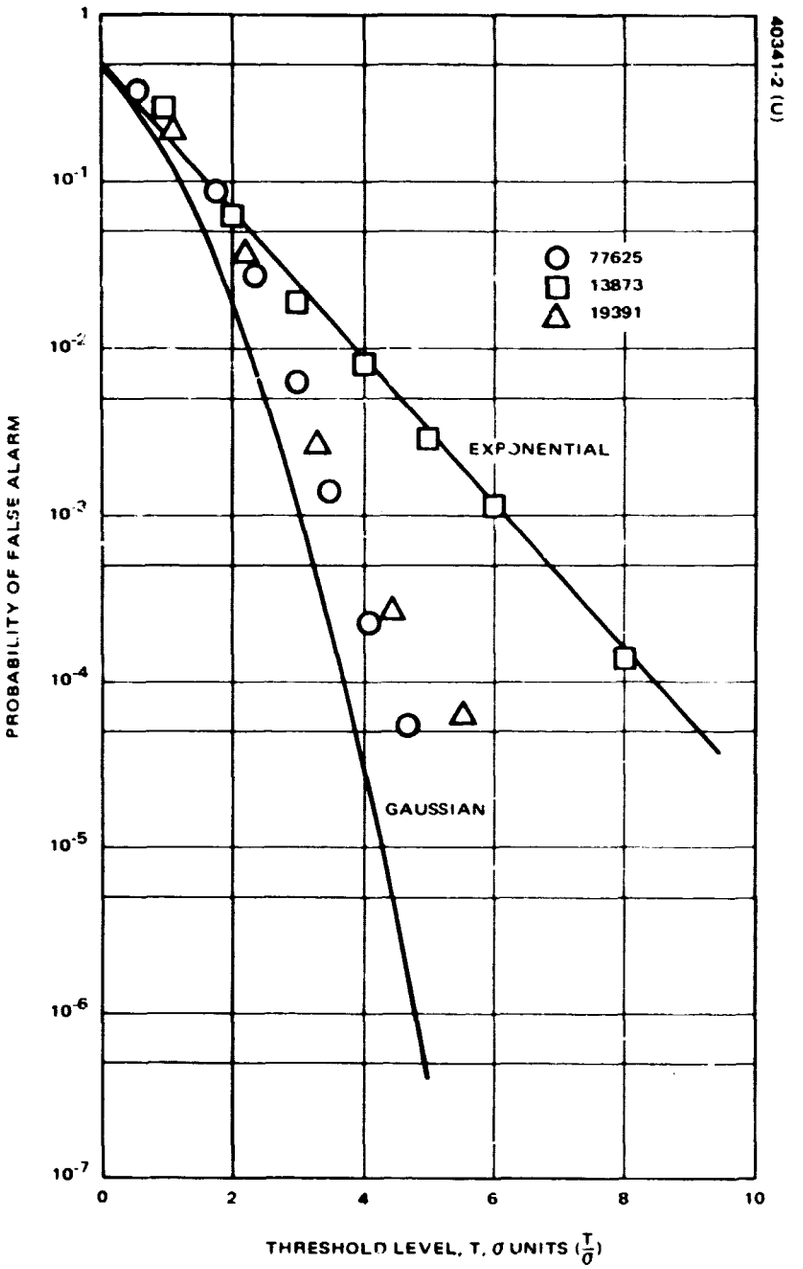

FIGURE 2-1. FALSE ALARM DATA FOR THREE PHOTOMULTIPLIER TUBES

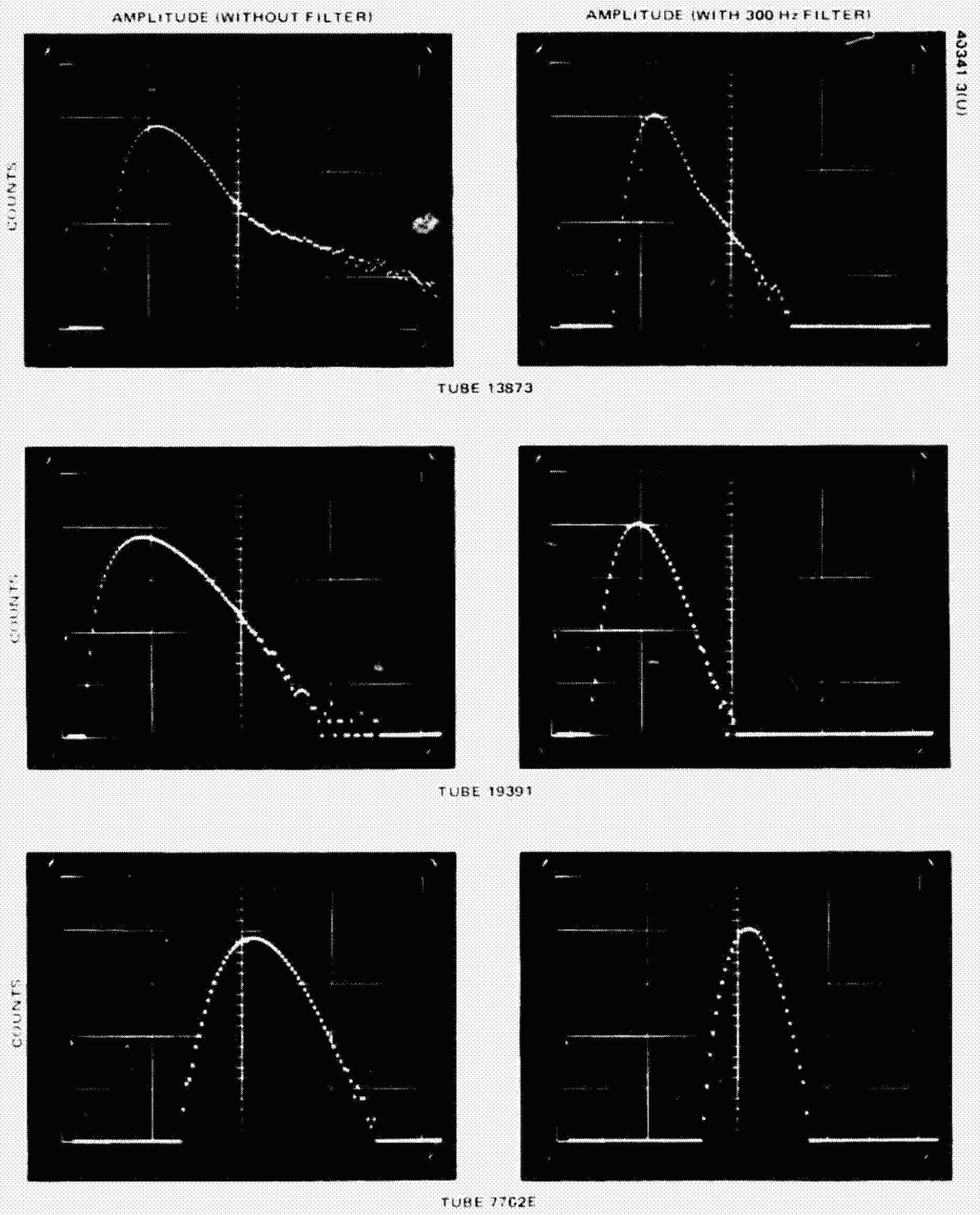

FIGURE 2-2. PHOTOMULTIPLIER BACKGROUND CURRENT AMPLITUDE DISTRIBUTION

as a function of their amplitude.

A Northern Scientific, Model NS-900-1A multichannel analyzer was employed for this direct photomulitplier dark and background distribution analysis. In addition a Tektronix 547 oscilloscope with a 1A7A plugin was utilized to produce a +B coincidence gate allowing the analyzer to be operated in a multichannel A/D conversion mode for analysis of the slowly varying filtered waveforms.

An examination of the data collected in this test (See Figure 2-2) confirms the previous conclusion that the distribution of large amplitude pulses differs markedly between tubes of the same family. Even after substantial filtering (300 hz bandwidth) some of the photomultipliers show an exponential form of tail distribution that is noticeably affecting the background distribution.

The exact cause of this variation in behavior among tubes is not known at this time. It is speculated that the presence of gas in the tubes may significantly affect these distributions, in particular, the large amplitude pulses.

2.3 Results and Conclusions

Figure 2-3 describes the several probability function distributions that have been discussed in this report for both the noise and signal + noise cases. Using these curves, the false alarm and missed pulse rates were computed for the exponential distribution as a worst case condition and for PMT 19391 as a more optimistic case that can probably be realized through photomultiplier tube selection. Tables 2-2 and 2-3 summarize the predicted false alarm and missed pulse rates as a function of threshold setting for the above two cases.

The signal to noise ratio of the STARS sensor as is used in the determination of its sensitivity and stability is given by

$$SNR = \frac{H_{eff}\ (V_p/V_{ss})}{\sigma'}$$

For the baseline design parameters, a SNR of 8.95 is obtained for the minimum required star.

It must be kept in mind that the performance characteristics described are a function of the angle between the pointing direction of the star tracker and the location of bright sources, which in this analysis was 15^{o} for the earth and 30^{o} for the sun. Performance will improve at greater angles until other sources become the limiting noise factor. In the SPACS program it was determined that galactic particles probably provide this lower limit.

In the course of the experimental portion of this study, the background source was turned off and a count was made of false alarms from all other sources. For a typical threshold setting, the count rate was around two orders of magnitude lower than that obtained with a bright source background.

In summary, this study indicates that as a worst case situation, a false alarm and missed pulsed rate of 75 per hour can be anticipated. A more optimistic, yet realistic condition predicts around 4 false alarms and missed pulses per hour. It should be noted from the probability values listed in Tables 2-2 and 2-3 that the occurrence of two consecutive perturbations has very low probability. It is also very obvious that an order of magnitude improvement is obtainable if desired (at the expense of electronic complexity) if time gating of the star pulses is applied as part of the signal processing.

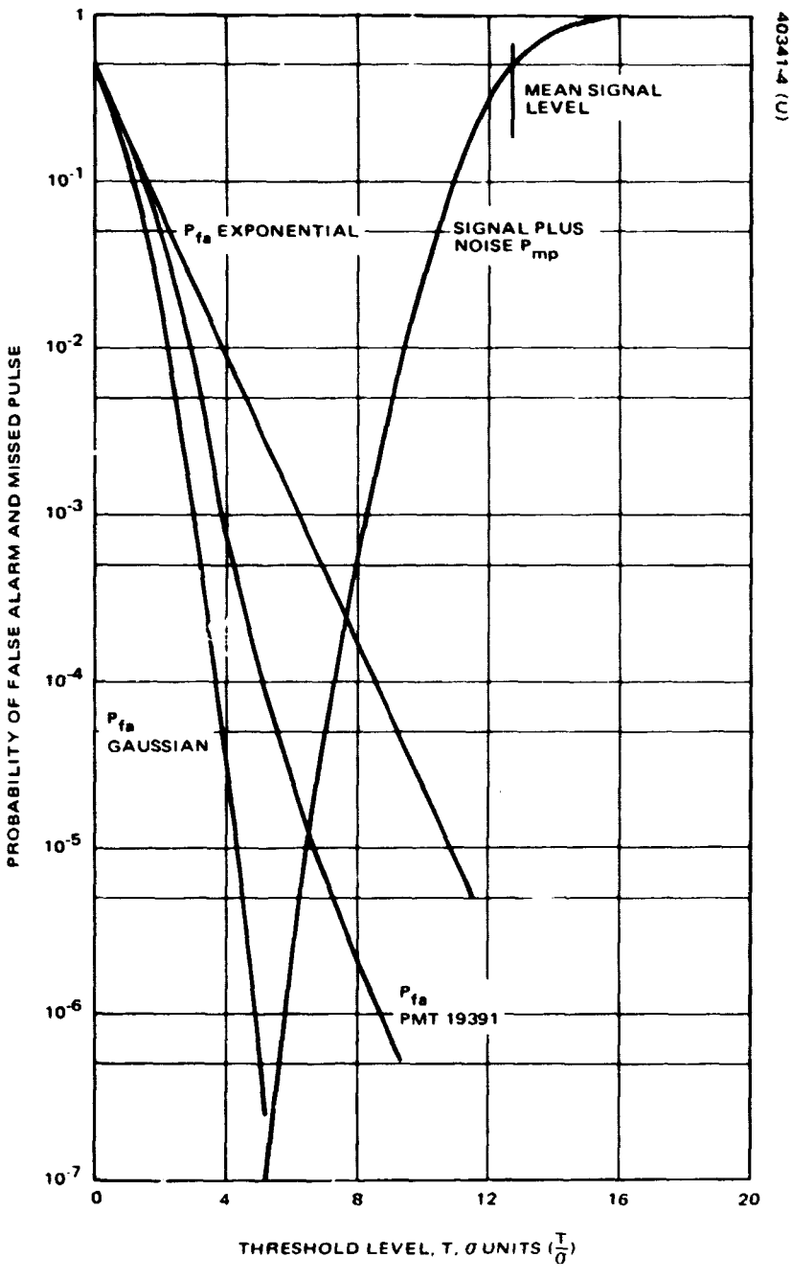

FIGURE 2-3. PROBABILITY OF FALSE ALARM AND MISSED PULSE AS FUNCTION OF THRESHOLD LEVEL

TABLE 2-2

False Alarm & Missed Pulsed Predictions. Exponential Case

Threshold	P_{fa}	FAR, hr^{-1}	P_{MP}	MPR, hr^{-1}
7σ	4.5×10^{-4}	565	3.5×10^{-5}	.505
8σ	1.65×10^{-4}	208	5.8×10^{-4}	8.35
9σ	6×10^{-5}	75	5×10^{-3}	72
9.2σ	5×10^{-5}	63	7.2×10^{-3}	104
9.5σ	3.5×10^{-5}	44	1.3×10^{-2}	187

TABLE 2-3

False Alarm & Missed Pulse Rates, PMT 19391

Threshold	P_{fa}	FAR, hr^{-1}	P_{MP}	MPR, hr^{-1}
6σ	2.4×10^{-5}	30	1.0×10^{-6}	.026
7σ	6.6×10^{-6}	8.2	3.5×10^{-5}	.505
$7.5\ \sigma$	3.5×10^{-6}	4.4	1.5×10^{-4}	2.16
$7.7\ \sigma$	3×10^{-6}	3.8	2.2×10^{-4}	3.2
7.8σ	2.75×10^{-6}	3.5	3.0×10^{-4}	4.3
8σ	2.2×10^{-6}	2.8	5.8×10^{-4}	8.35

3. Attitude Control System Design

3.1 Spacecraft Dynamics

The spacecraft dynamics used in the simulation included nonlinear dynamics to obtain a more accurate representation of the spacecraft dynamics for the STARS application. The high degree of accuracy desired in the dynamics model complements the high degree of accuracy expected from STARS. Nonlinear terms as well as product of inertias are included in the analysis to formulate a more representative dynamics model of the spacecraft.

The inertia matrix for the spacecraft is shown below. The coordinates, x, y, z are inertially referenced general orthogonal coordinates.

$$I = \begin{bmatrix} I_{xx} & -I_{xy} & -I_{xz} \\ -I_{zy} & I_{yy} & -I_{yz} \\ -I_{zx} & -I_{zy} & I_{zz} \end{bmatrix}$$

where

$$I_{ij} = -\int i \cdot j \, dm$$

$$I_{ii} = \int (j^2 + k^2) \, dm$$

i, j, k = coordinates, origin c.g.

m = mass

The angular velocity and acceleration matrices for the vehicle are

$$\bar{\omega} = \begin{bmatrix} \omega_x \\ \omega_y \\ \omega_z \end{bmatrix}, \quad \dot{\bar{\omega}} = \begin{bmatrix} \dot{\omega}_x \\ \dot{\omega}_y \\ \dot{\omega}_z \end{bmatrix}$$

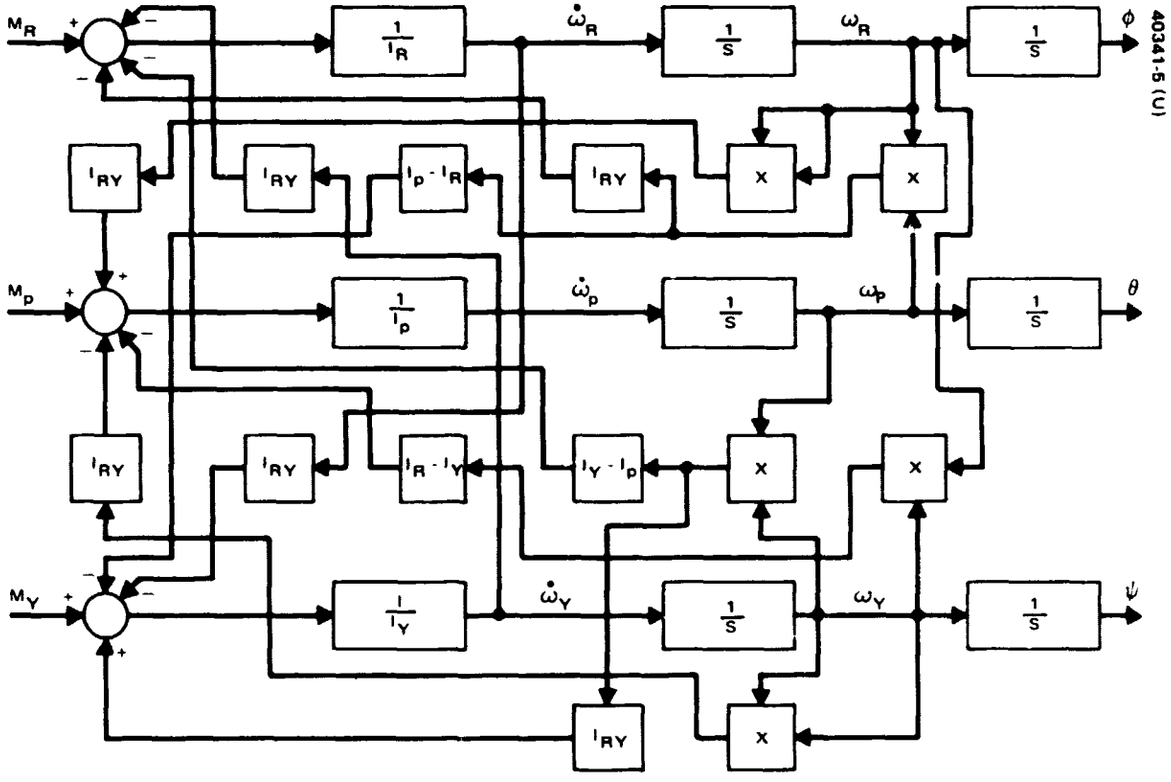

FIGURE 3-1. BLOCK DIAGRAM FOR VEHICLE DYNAMICS

where $\omega_q = \frac{d\theta_q}{dt}$ θ = angle rotation about q-axis, q = x, y, z

The moment torque equation is

$$\bar{M}_{cg} = \dot{\bar{H}} + \bar{\omega} \times \bar{H}$$

where $\bar{H} = I\,\bar{\omega}$

The moment equation for the EOS vehicle can be calculated to be (See Appendix 5-1)

$$M_R = I_R \dot{\omega}_R + I_{RY} \dot{\omega}_Y + I_{RY} \omega_P \omega_R + I_Y \omega_P \omega_Y - I_P \omega_P \omega_Y$$

$$M_P = I_P \dot{\omega}_P - I_{RY} \omega_R^2 - I_Y \omega_R \omega_Y + I_R \omega_R \omega_Y + I_{RY} \omega_Y^2$$

$$M_Y = I_Y \dot{\omega}_Y + I_{RY} \dot{\omega}_R + I_P \omega_R \omega_P - I_R \omega_R \omega_P - I_{RY} \omega_P \omega_Y$$

Figure 3-1 shows the block diagram for the spacecraft dynamics based on the set of equations above. The torque exerted on the spacecraft produces roll, yaw, and pitch angles ϕ, Ψ, and θ, respectively. The torque input is supplied by the control system that receives attitude error information from STARS. The spacecraft attitude angles, ϕ Ψ, and θ are then reflected in the errors sensed by the star sensor/telescope.

3.2 Disturbance Torques

Sources of disturbance torques on an earth satellite are environmental (external) or internal. Those sources, due to interactions of the spacecraft with the environment, are gravitational gradient, solar-radiation pressure, aerodynamic pressure, meteorite impact and magnetic interaction between the earth's field and spacecraft electric currents. Internal sources are the

expulsion of matter (e.g., thrusters), activation of spacecraft elements or appendages and interaxis coupling.

Disturbance torques can be either cyclic or secular as referenced from inertial space. Momentum storage devices (e.g., reaction wheels) can be utilized to accommodate angular momentum due to cyclic disturbance without requiring unloading and exceeding minimal attitude error. Secular torques require unloading of stored momentum periodically because of continuous momentum buildup.

SOLAR PRESSURE TORQUE

The resultant solar pressure torque is a function of the effective area of the spacecraft exposed to the sun, the reflectivities of the exterior surfaces, and the distance between the center of mass and center of pressure.

The basic equations for solar pressure forces are:

$$\bar{F}_i = -P_o \left[\int_{A_i} (1 + \nu_i \mu_i) \boxed{\hat{v} \cdot \hat{n}} (\hat{v} \cdot \hat{n}) \hat{n} \, dA_i \right. \qquad \text{(Normal Forces)}$$

$$+ \int_{A_i} (1 - \nu_i \mu_i) \boxed{\hat{v} \cdot \hat{n}} (\hat{n} \times \hat{v} \times \hat{n}) \, dA_i \qquad \text{(Shear Forces)}$$

$$\left. + \int_{A_i} \frac{2}{3} \nu_i (1 - \mu_i) \boxed{\hat{v} \cdot \hat{n}} \hat{n} \, dA_i \right] \qquad \text{(Diffuse Reflection Forces)}$$

where the terms are given as:

ν_i = reflectance coefficient over the ith surface

μ_i = diffusivity coefficient over the surface (μ_i = 1 for specular reflection)

$\hat{n}$ = unit vector directed outward normal to dA_i

ρ_o = solar radiation pressure constant for the normal incidence ($\hat{v}.\hat{n}$) = 1 and complete absorptivity (ν = 0) = 9.4×10^{-8} pound/foot^2

A_i = the area of the ith surface

$\hat{v}$ = unit vector directed to sunline

The torque produced by the solar radiation pressure is

$$\bar{T}_s = \sum_i \int_{A_i} \ell_i \times \bar{F}_l \, dA_i$$

where ℓ_i is a vector from the vehicle center of mass to the surface (dA_i) center of pressure.

Normal force effects were considered adequate for the generalized EOS spacecraft configuration used in the study. The solar panel is sun oriented and contributes heavily to the normal force, while the remaining surfaces tend to produce cancellation of shear force and/or have low effective reflectances.

The maximum solar pressure torque has been calculated to be 1.0×10^{-5} foot-pound for the 9:00 A.M. orbit.

For the computer simulation, the sun line is assumed to be along the vernal equinox and the spacecraft is assumed to be symmetric about the pitch axis such that the center of pressure is located along the pitch axis. Torque about each axis is approximated by a sinusoid based on the orbit rate. The approximations used are:

$$T_{Roll} = 1.0 \times 10^{-5} \cos \omega_o t \text{ foot-pound}$$

$$T_{Pitch} = 0.0 \text{ foot-pound}$$

$$T_{Yaw} = 1.0 \times 10^{-5} \sin \omega_o t \text{ foot-pound}$$

where

$$\omega_o \approx 10^{-3} \text{ radian/second}$$

The solar torque presented above should provide a representative disturbance torque for observing STARS performance.

AERODYNAMIC PRESSURE TORQUE

The aerodynamic pressure effect on the spacecraft at an altitude of 1000 km produces a torque on the order of 2×10^{-6} foot-pound, primarily in the pitch direction for an angle of attack of eight (8) degrees. The general equation for aerodynamic torque is

$$T_A = P_A A_A (X_{cg} - X_{cp}) \sin \alpha$$

where

T_A = torque due to aerodynamic pressure, foot-pound

P_A = atmospheric pressure, pound/foot^2

A_A = surface area exposed to aerodynamic pressure, foot^2

α = vehicle angle of attack, radians

Compared to solar pressure torque, aerodynamic pressure torque is small.

GRAVITY GRADIENT TORQUE

A spacecraft with non-equal principal moments of inertia tends to align itself in the gravity field so that its principal axis of minimum inertia lies along the gravitational vertical. The torque components due to gravity gradient are

$$T_{g \text{ roll}} = \frac{-3}{2} \omega_o^2 (I_p - I_Y) \sin 2\phi$$

$$T_{g \text{ pitch}} = \frac{-3}{2} \omega_o^2 (I_R - I_Y) \sin 2\theta$$

$$T_{g \text{ yaw}} = 0$$

where $\omega_o \cong 10^{-3}$ radian/second orbital rate

I_R, I_P, I_Y are the vehicle moments of inertia about roll, pitch and yaw, foot-pound-second^2; ϕ and θ are the roll and pitch error angles, radians.

The gravity gradient effect produces a torque about the pitch axis equal to 2.6×10^{-8} foot-pound, which is small compared to the solar pressure torque.

MAGNETIC PRESSURE TORQUE

The magnetic field of the earth exerts magnetic pressure on the spacecraft through an interaction with electric currents on the spacecraft. The torque applied to the spacecraft is given by

$$\overline{T} = 6.86 \times 10^{-6} \overline{M} \times \overline{B} \quad \text{foot-pound}$$

where

$\overline{M}$ = magnetic moment, amp-turn-foot^2

$\overline{B}$ = magnetic flux density due to earth's magnetic field, gauss

The magnitude of the earth's magnetic field can be expressed as

$$B = \frac{1.43 \times 10^{10}}{r^3} (\sin^2 \psi + 4 \cos^2 \psi)^{1/2}$$

where

r = distance from dipole center to field point, radius of orbit (nautical miles)

ψ = angle r makes with the earth's north-south dipole centerline (radians) or $\psi = \omega_o t$ where ω_o is the orbit rate.

The distance r is the sum of the earth's radius (3444 nm) and h_1 the altitude of the orbit. For an altitude of 540 nm, the magnetic flux density of the earth is 4.6×10^{-3} gauss. Assuming 600 ampere-turns-foot^2 for the spacecraft's magnetic moment, the peak value of magnetic pressure torque is 1.9×10^{-5} foot-pound. The torque varies with position along the orbit.

3.3 Compensation

The vehicle control subsystem that receives attitude reference data from the STARS sensor and gimbal subsystems must provide the proper compensation for the overall STARS attitude control system in order for the vehicle's response to be stable and have the desired pointing characteristics. The compensation that provides the control law for this system has two major tasks; it must hold the vehicle pointing error due to disturbance torques to within $\pm$.20 arcseconds, and it must also attenuate the STARS sensor noise. The disturbance torques acting on the vehicle occur at orbit frequency, while the STARS sensor noise occurs at frequencies a couple of magnitudes higher than orbit frequency.

A simplified block diagram of the overall STARS attitude control system is shown below.

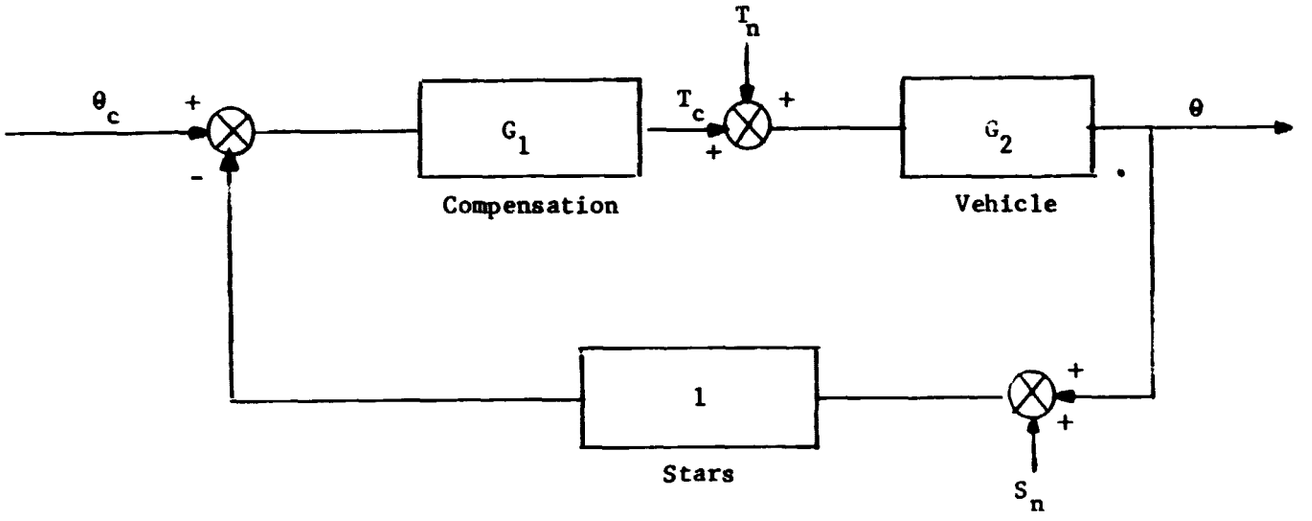

The requirement that the vehicle pointing error due to maximum disturbance torques is less than .20 arcseconds; places a magnitude contraint on the transfer function, θ/T_N

$$\left| \frac{\theta\ (j\ \omega)}{T_n\ (j\ \omega)} \right| = \frac{10^{-6}}{10^{-5}} = \frac{1}{10}\ \frac{\text{radian}}{\text{foot-pound}}$$

From the figure

$$\frac{\theta\ (j\ \omega)}{T_n\ (j\ \omega)} = \frac{G_2\ (j\ \omega)}{1 + G_1\ (j\ \omega)\ G_2\ (j\ \omega)}$$

$$\left| \frac{G_2\ (j\ \omega)}{1 + G_1\ (j\ \omega)\ G_2\ (j\ \omega)} \right| = \frac{1}{10}$$

$$\left| G_1\ (j\ \omega) \right| = 10 - (1/|G_2(j\omega)|)$$

This expression yields a gain of 10 for G_1 at orbit frequency. To reduce pointing error due to STARS sensor noise, the gain of θ/T_n should be made as small as possible at the higher frequencies. With these gain constraints and other considerations in mind, the following compensation was chosen:

$$G_1(s) = \frac{K(\tau_1 s + 1)^2}{s(\tau_2 s + 1)}$$

$K = .01$ foot-pounds/radian

$\tau_1 = 67$ seconds

$\tau_2 = 6.7$ seconds

The gain K is chosen, as described above, to achieve the required pointing accuracy in the presence of disturbance torques. The double lead is required to obtain sufficient gain and phase margins for system stability. An integrator was added to alleviate a steady-state error, a result of the annual precession of the orbit plane about the center of the earth, which was encountered during simulation. The lag is used to produce a roll off at higher frequencies to filter out STARS sensor noise.

3.4 Control System Configuration

The control system torques the spacecraft to produce attitude changes. Torquing can be produced by momentum exchange between the vehicle and a momentum storage device, such as the reaction wheel. Three reaction wheels can be used to handle three attitude angles of the spacecraft.

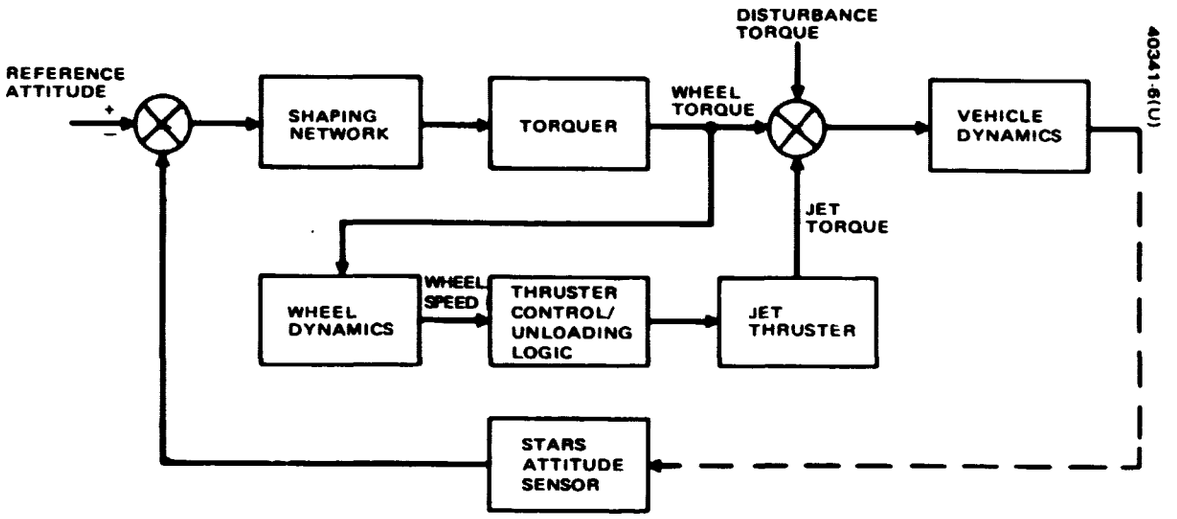

FIGURE 3-2. CONTROL SYSTEM CONFIGURATION

Other means of applying torque are available, but for the sample example of torquing separately in each of the three axis and of making use of the cyclic nature of torque disturbance from the environment, the reaction wheel torquing system is a good candidate. Jet thrusters are also used, and they transfer momentum from the wheels during the unloading of the wheel momentum.

The control that produces signals to command the reaction wheel includes a shaping network or compensation to give good control characteristics to the control system. The compensation is designed to attenuate sensor noise and to enable the control system to maintain $\pm$.20 arcsecond vehicle pointing accuracy under the effects of disturbance torques.

The simulation uses this relatively simple control law. The results show that this control law is effective in providing good response characteristics in controlling the nonlinear spacecraft dynamics. Figure 3-2 shows the control system configuration. Included in the figure is the logic box for unloading the wheels. Various torques that the vehicle experiences are also shown.

The use of a relatively simple control law was desirable to show that STARS can operate with a simple control system rather than only with a limited and/or complex type of control law. The use of a simple control law also allows for the use of more specific or precise control, if needed. A more complex control law can be designed to handle more difficult control problems if such problems should arise.

4. Performance Analysis and Simulation

4.1 Precision Gimbal System

Figure 4-1 shows the configuration of the precision gimbal pointing control system. This configuration is identical for both the pitch and polar axes.

The command to the system (θ_c) is a binary number that represents the desired gimbal position which is calculated on board and updated at predetermined intervals using ephermis data. The actual position of the gimbal is monitored by use of an Inductosyn. The output of the Inductosyn, a binary signal, is fedback and a binary subtraction is made between this signal and the command. The resulting error signal is passed first through a digital to analog converter and then through a shaping network. The output of the shaping network is a voltage that drives an Inland brush dc motor which positions the gimbal shaft. The positioning of the gimbal shaft by the motor is corrupted by bearing noise. This bearing noise which is due to mechanical tolerances and some uncertainties is described in Table 4-1. The other noise source in the gimbal system is on the Inductosyn's measurement of the actual gimbal position. This is described in Table 4-2. Both noise sources are assumed to be white with zero mean.

4.1.1 Pitch Gimbal Simulation

The pitch gimbal servo is used to unwind the orbital rate of the spacecraft about the earth; this must be performed in order to maintain the pitch axis of the telescope fixed in inertial space. The command angle to the pitch servo is the orbital rate of the spacecraft about the earth. This command is approximately 240 arcseconds per second and is updated every .015 seconds. Due to this relatively high angular rate and to the high load inertia of the pitch axis, a stick-slip friction model can be avoided and

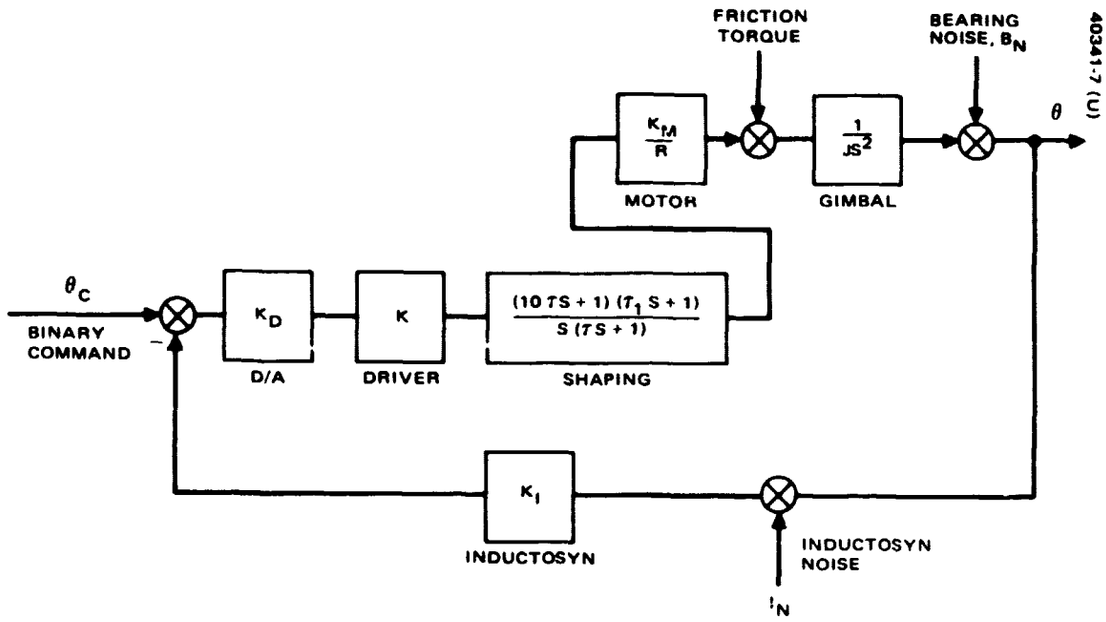

PARAMETERS:

K_D = 6.25×10^{-3} $\frac{\text{Volts}}{\text{bit}}$

K_I = 0.404 $\frac{\text{bit}}{\text{arcsec}}$

K_M = 0.376 $\frac{\text{ft-lb}}{\text{Ampere}}$

R = 13 Ω

T = 0.01 sec

T_1 = 1.0 sec

J = { 1.5 slug-ft^2 – PITCH AXIS; 0.05 slug-ft^2 POLAR AXIS }

K = { 200 VOLTS/VOLT – PITCH AXIS; 0.80 VOLTS/VOLT – POLAR AXIS }

B_N = GAUSSIAN DISTRIBUTION, MEAN = 0, VARIANCE = 1.137 arcsec

I_N = GAUSSIAN DISTRIBUTION, MEAN = 0, VARIANCE = 1.720 arcsec

FIGURE 4-1. PRECISION GIMBAL SYSTEM

TABLE 4-1
BEARING NOISE

Item	Error Class*	Error Quantity	Definition	Assigned Value Maximum, microinches	Angular** Contribution in Assembly, microradians	Remarks
1	E	L (IRB-IRG)e	Eccentricity. Inner race groove to inner race bore (TIR)	60	Not applicable	Each inner race marked with high spot. High spots of bearing pair aligned, thus causing residual error due to a) magnitude difference between race eccentricities and b) deviation in true high spot location and alignment.
2	RE	L (IRB-IRG)e	Residual error of 1	15	$\frac{15}{10} = 1.5$	
3	U	L (IRB-IRG)e	Uncertainty of 1	15	$\frac{15}{10} = 1.5$	Uncertainty in (E) L (IRB-IRG)e measurement.
4	U	L (IRRF-IRG)AW	Orthogonal component (radial direction). Axial wobble of inner race groove to inner race reference face	7.5	$\frac{15}{10} = 1.5$	Axial wobble high spot rarely coincides with eccentricity high spot so that correction cannot be made simultaneously for wobble. Assumed worst case for opposite bearing pairs diametrically opposed; however, mean was assumed within each bearing pair.
5	U	L (B-B)V	Variance. Ball-to-ball diameters (for bearing ball complement)	5	$\frac{10}{10} = 1.00$	Assuming: larger balls (1/2 of the complement) diametrically oppose smaller balls. Worst possible case – both bearing pairs.
6	U	L PC	Size of particulate contamination	45	$\frac{45}{10} = 4.5$	Assuming: some particles at times enter ball to race contact and not necessarily simultaneously in both bearings and pairs in diametrically opposed locations.
7	E	L (SH-IR)f	Fit between inner race bore and shaft	Interference	0	Interference to exist over entire operational thermal range.
8	E	L (H-OR)f	Fit between outer race and housing	Interference	0	
9	E	$L(B_1-B_2)e$, SH	Shaft eccentricity between bearing locations 1 and 2 (TIR)	60	Not applicable	Combined with item 1, races are angularly positioned to minimize effective total eccentricity; i.e., shaft rotational axis defined by race grooves.
10	RE	L [(#1-#9)] e, SH	Residual error of shaft axis definition (1 and 9 combination)	30	$\frac{30}{10} = 3$	
11	U	L [(#1-#9)] e, SH	Uncertainty of shaft axis definition (1 and 9 combination)	15	$\frac{15}{10} = 1.5$	
12	U	L [(#1-#9)] e, SH, TH	Uncertainty in 1 and 9 combination due to nonhomogeneous response to thermal changes***	2.5	$\frac{5}{10} = 0.50$	Thermal differential expansion induced change in initial interference fits may not take place equally everywhere due to nonhomogeneity of structures and materials.
13	U	L_{BC} [IR-OR] e, TH	Ball contact position change due to outer race to inner race thermal condition change	2.5	$\frac{5}{10} = 0.50$	Even if both inner and outer races experience identical change in temperature (no gradient) and if both bearings experienced identical change, larger outer race will change at a higher rate than inner race. Contact angle shifts. Assume: bearing pair (1) experiences thermal shift larger or smaller than that experienced by bearing pair (2) this causes angle uncertainty (13) due to difference in race curvatures and ball sizes between bearing pairs (1) and (2).
14	U	L (OR-HSG)e, TH	Housing to outer race induced eccentricity change due to nonhomogeneous interference fit change due to thermal variations	2.5	$\frac{5}{10} = 0.50$	Original outer race and housing errors (as assembled) are lumped in an offset angle error – a constant. However, if changes occur, the offset angle changes in an unpredictable manner.
15	U	I_{DS}(LE)	Uncertainty due to launch environment caused Brinell spots	30	$\frac{30}{10} = 3.0$	75% Brinell spot depth of indentation in one bearing, taking total load in radial direction, (60 g peak acting for > 1 second).

*E: error, RE: residual error, and U: uncertainty.
**1 microradian = 0.206 arcsec.
***Bulk temperature variation limited to ± 10°F; radial gradient limited to 5°F maximum.

TABLE 4-1

(CONTINUED)

Item	Error Quantity, microradians	Quantity Squared, microradians	Extension
		SUMMARY	
2	1.5	1.5	Σ = 5 (errors)
10	3.0	9.0	Rss = 3.24 microradians
			~0.7 arcsec
3	1.5	2.25	Σ = 37.8 (uncertainties)
4	1.5	2.25	Rms = $\sqrt{\frac{37.8}{Q-1}}$
5	1.00	1.00	
6	4.5	20.3	Σ = 2.17 microradians
			~0.45 arcsec
11	1.5	2.25	
12	0.50	0.25	
13	0.50	0.25	
14	0.50	0.25	
15	3.0	9.00	

Therefore: Total error and uncertainty contributions (maximum) =

0.70 + 0.45 = 1.15 arcsec

TABLE 4-2

INDUCTOSYN ERRORS

A.	Errors systematic with poles (512 per revolution)	0.45 arcseconds
B.	Errors systems per revolution	
1.	Centering indication on Inductosyn discs	0.68
2.	Effect of bearing bias	0.50
3.	Rotor to housing alignment	1.00
4.	Stator to shaft alignment	1.00
5.	Wobble	0.20
6.	Bearing random effect	0.10
RSS TOTAL		1.72 arcseconds

a conventional coulomb friction model used.

A separate computer simulation of the pitch gimbal servo was performed using the MIMIC language. The computer listing of this pitch simulation can be found in Appendix 5.2. Because the command angle to the pitch gimbal is updated every .015 seconds, a very small integration step is required, thus only short simulation runs (approximately 20 seconds) were economically feasible. The pitch gimbal system response is shown in Figures 4-2, 4-3, and 4-4. In all three figures, the independent axis is scaled to seconds of time and the dependent axis is scaled to arcseconds.

Figure 4-2 shows both the command angle (dashed line) and the actual angle (solid line) as a function of time. Both curves lie on top of one another, making the gimbal error barely visible on this scale. Figure 4-3 shows the difference between the command angle and the actual angle on a much smaller scale. The gimbal error is seen to stay almost completely within a plus or minus two arcsecond error band. The RMS value of the gimbal pointing error is shown by Figure 4-4 to be 1.2 arcseconds. This pointing error is obviously well within the 1.80 arcescond error budget allotted to each gimbal system.

4.1.2 Polar Gimbal Simulation

The polar axis servo is used to unwind the annual precession of the orbit plane, which must be performed in order to maintain the polar axis of the telescope fixed in inertial space. The command to the polar axis servo corresponds to a one revolution or 360 degrees per year rate. This command is updated only every 90 seconds. Unlike the pitch gimbal, the slow rotation and small angle incremental motion of the polar gimbal cause

an elastic behavior between the moving surfaces of the gimbal. As a consequence, the polar gimbal simulation utilizes an elastic friction model, based on experimental data obtained on another Hughes program. Figure 4-5 shows the elastic friction characteristics observed on the Hughes OSO Program. The STARS polar gimbal operating region is shown in the lower left hand portion of the figure. For this region, the friction torque is directly proportional to the angular displacement. The elastic friction model that was used in the simulation is shown in the right half portion of the same figure. The elastic friction torque in the simulation model is equal to $K_{\cdot}$ times $\Delta\theta$, when $\Delta\dot{\theta}$ is not equal to zero, and zero when $\Delta\dot{\theta}$ is equal to zero. Where $\Delta\theta$ is the incremental change in the command at each update interval.

A separate computer simulation of the polar gimbal servo was performed using the MIMIC language. The computer listing can be found in Appendix 5.2. Figures 4-6, 4-7, and 4-8 show the polar gimbal system response. In all three figures, the independent axis is scaled to seconds of time and the dependent axis is scaled to arcseconds.

Figure 4-6 shows both the command angle (dashed line) and the actual angle (solid line) as a function of time. The gimbal angle is seen to follow the staircase type motion of the command angle; however, its amplitude is corrupted by noise. Figure 4-7 shows the error between the commanded angle and the gimbal's actual position. Most of the error is seen to fall into a plus or minus 2 arcsecond region about zero. Figure 4-8 shows the RMS value of the pointing error to be 1.80 arcseconds, which is exactly the allotted amount of error for the polar gimbal system.

The pitch and polar gimbal simulations described above demonstrate that the precision gimbal of Figure 4-1 can meet the high accuracy requirements of STARS.

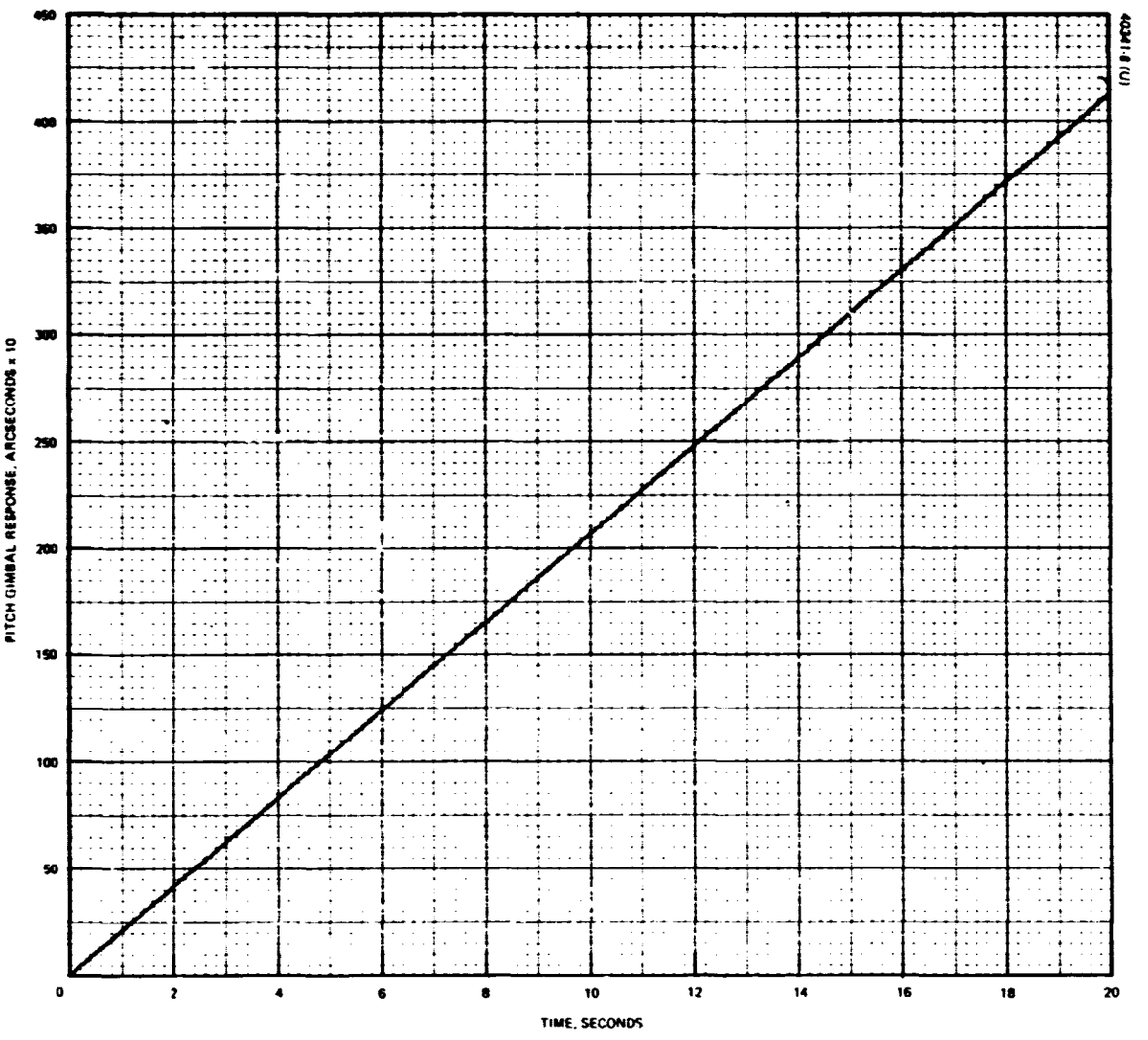

FIGURE 4-2. PITCH GIMBAL RESPONSE

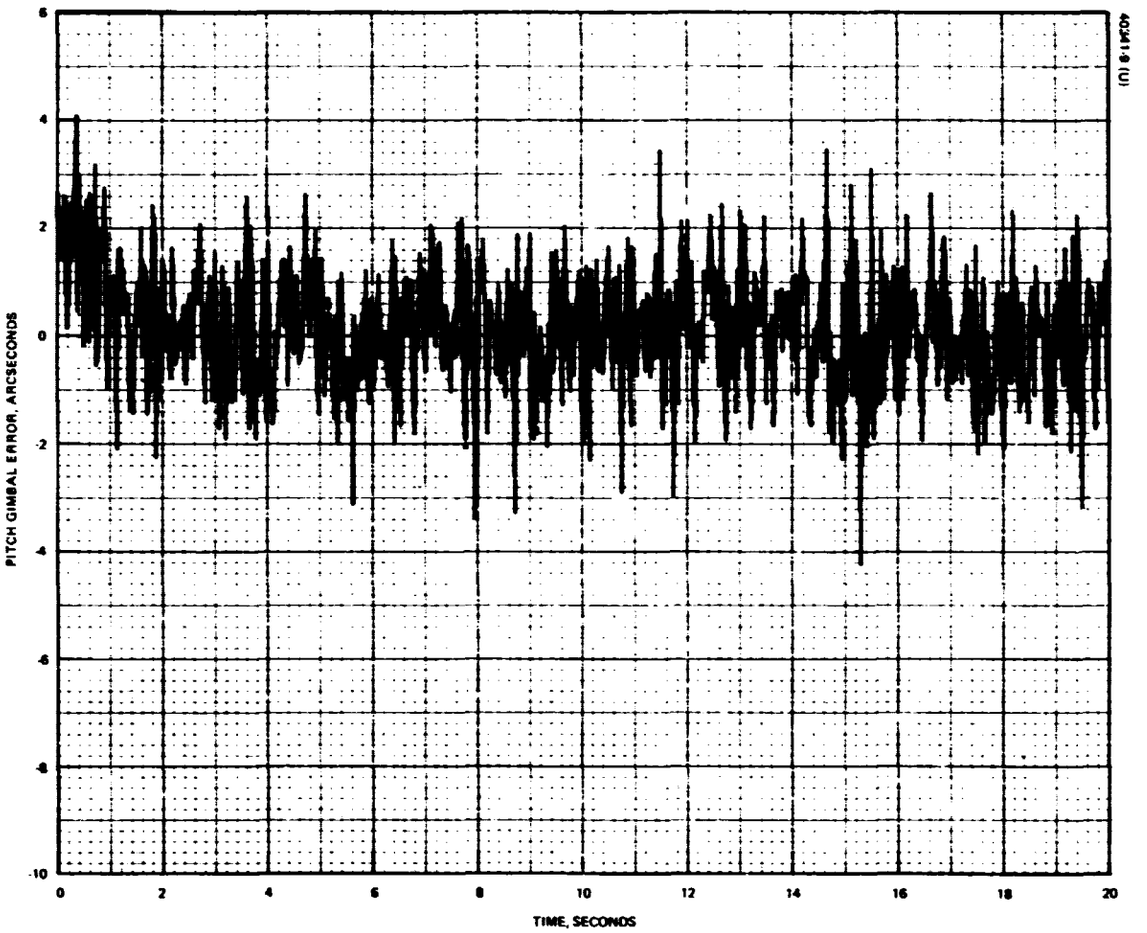

FIGURE 4-3. PITCH GIMBAL ERROR

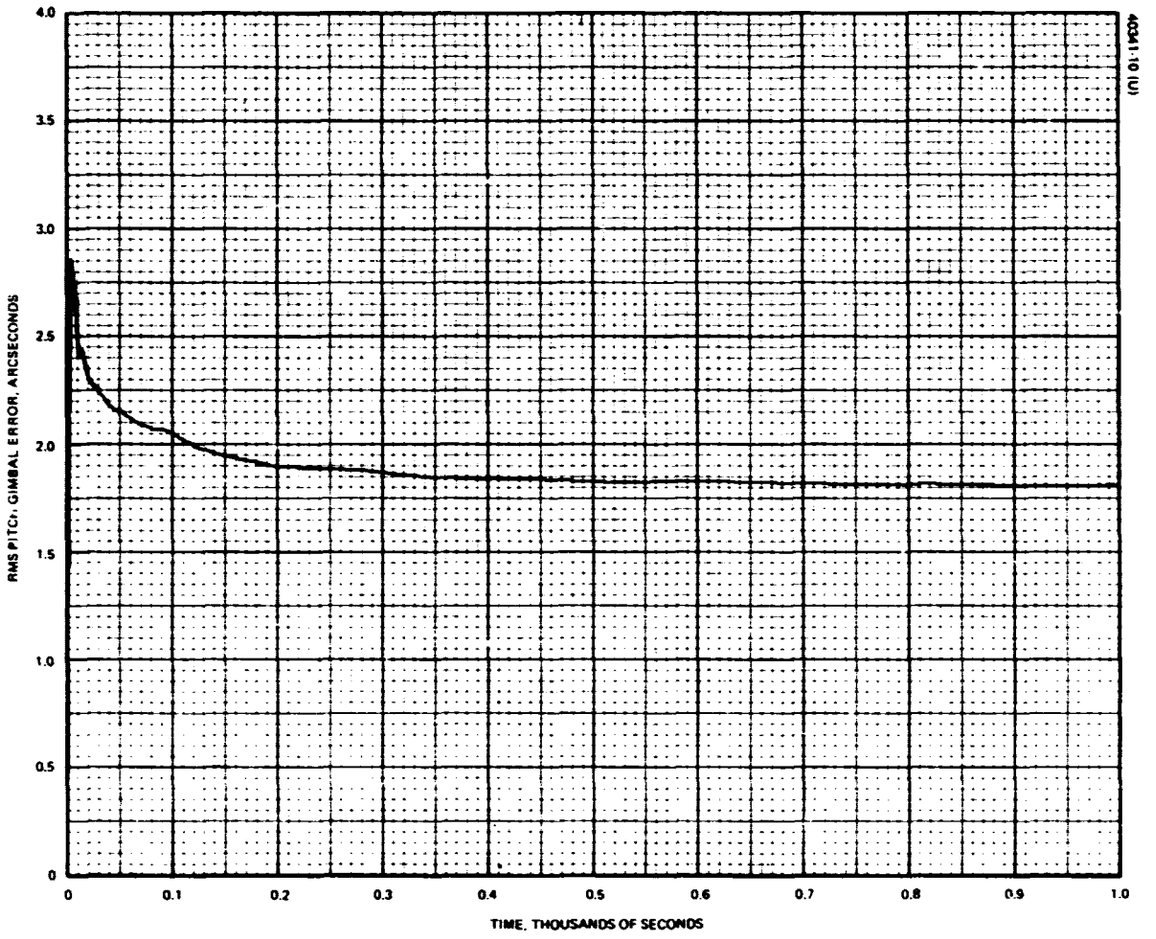

FIGURE 4-4. RMS PITCH GIMBAL ERROR

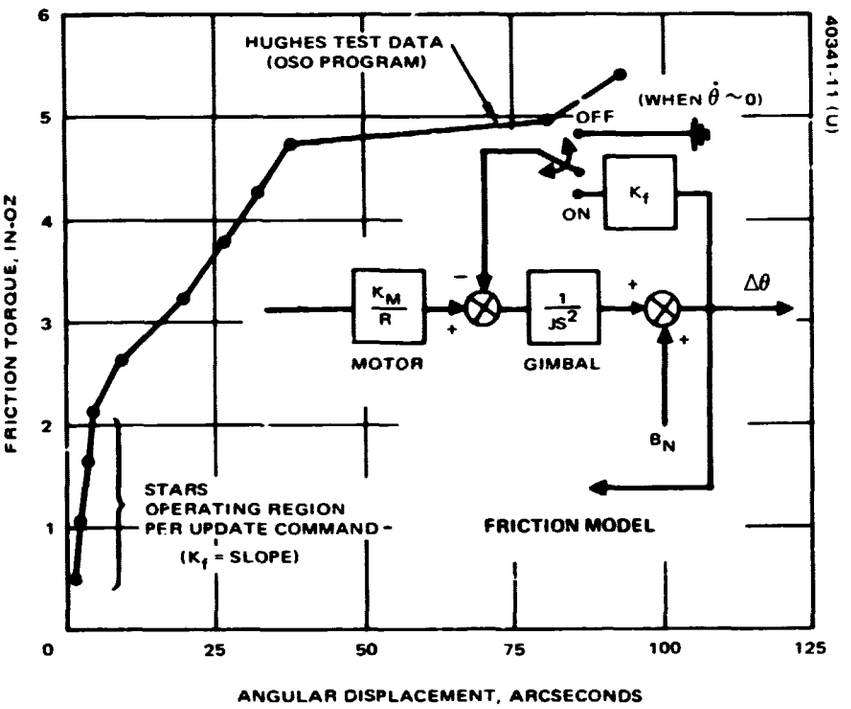

FIGURE 4-5. ELASTIC FRICTION CHARACTERISTICS

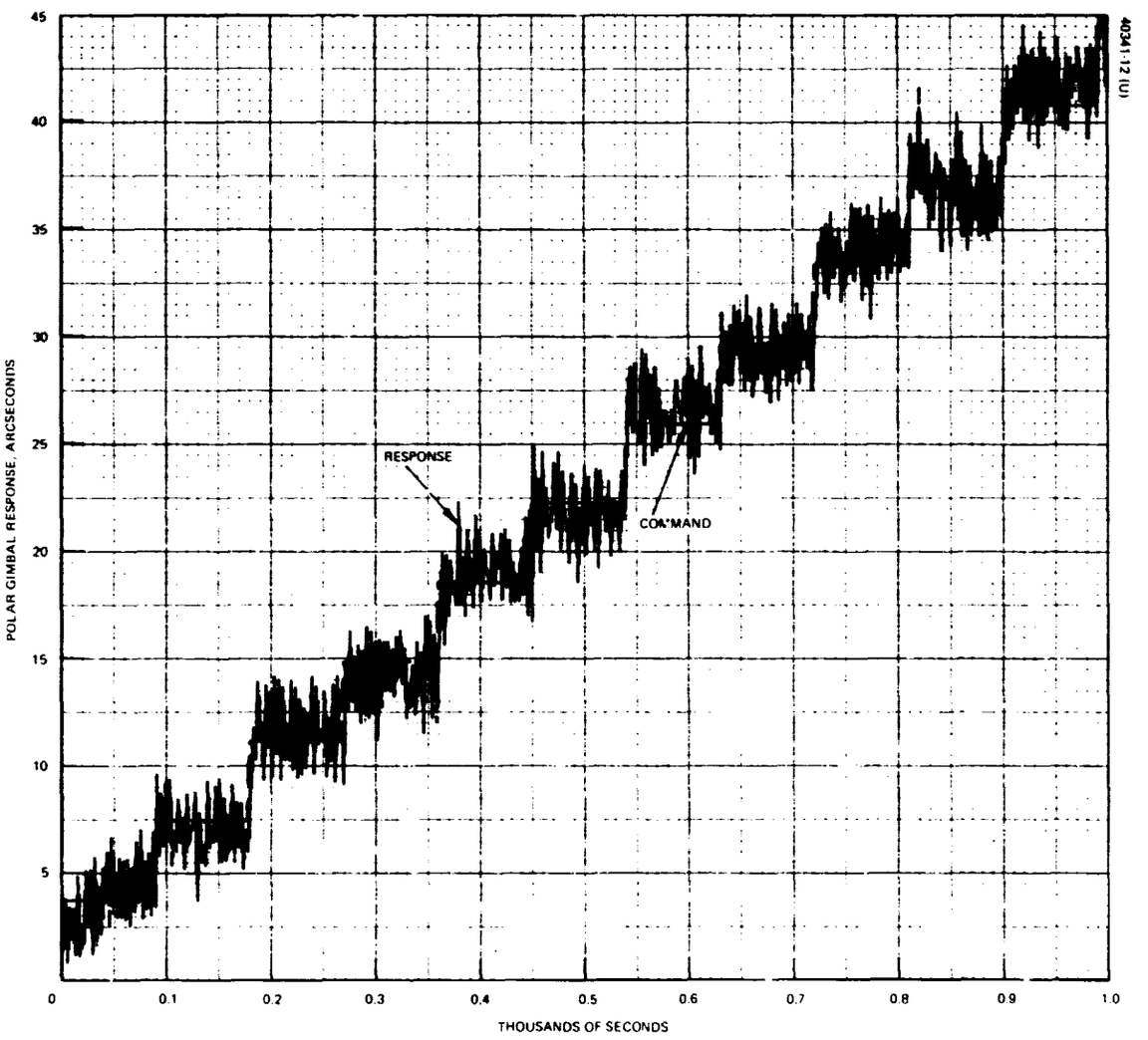

FIGURE 4-6. POLAR GIMBAL RESPONSE

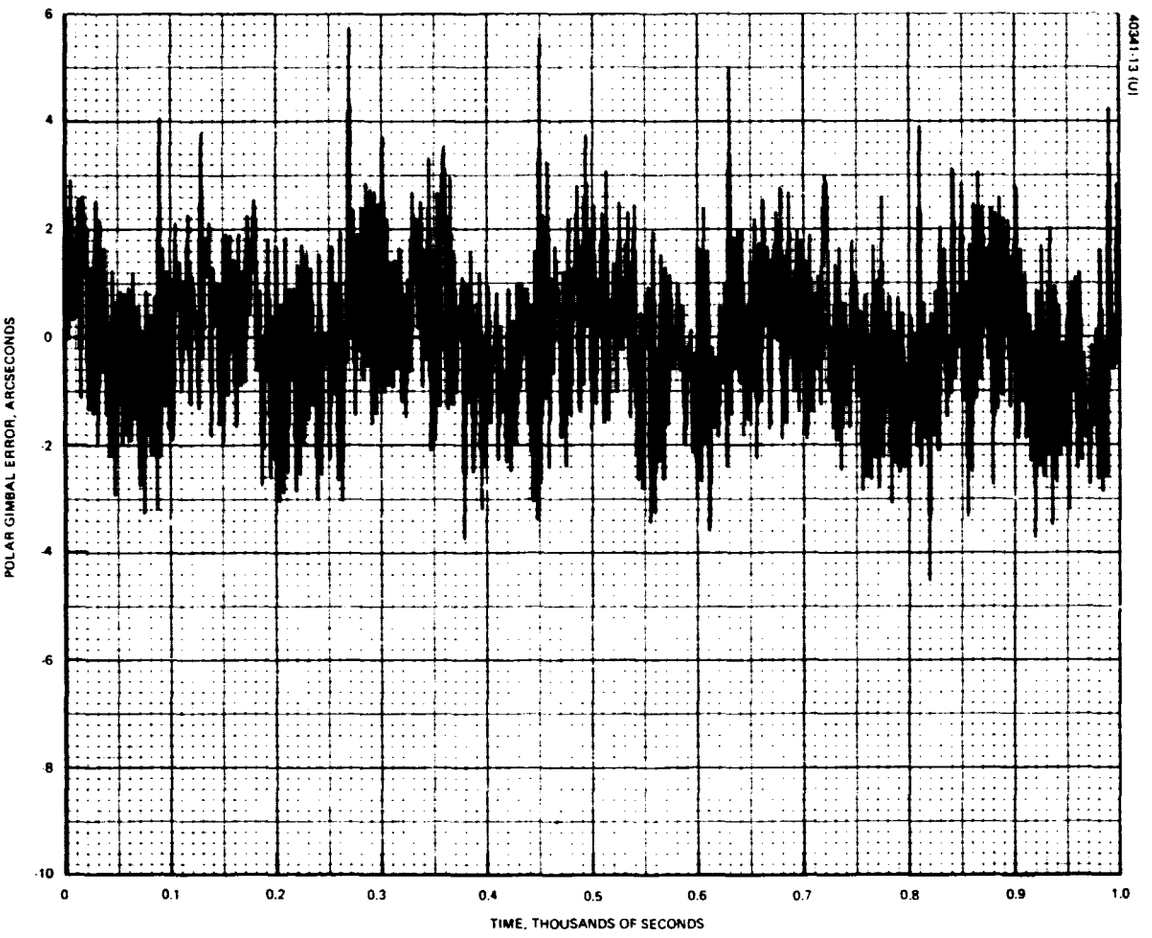

FIGURE 4-7. POLAR GIMBAL ERROR

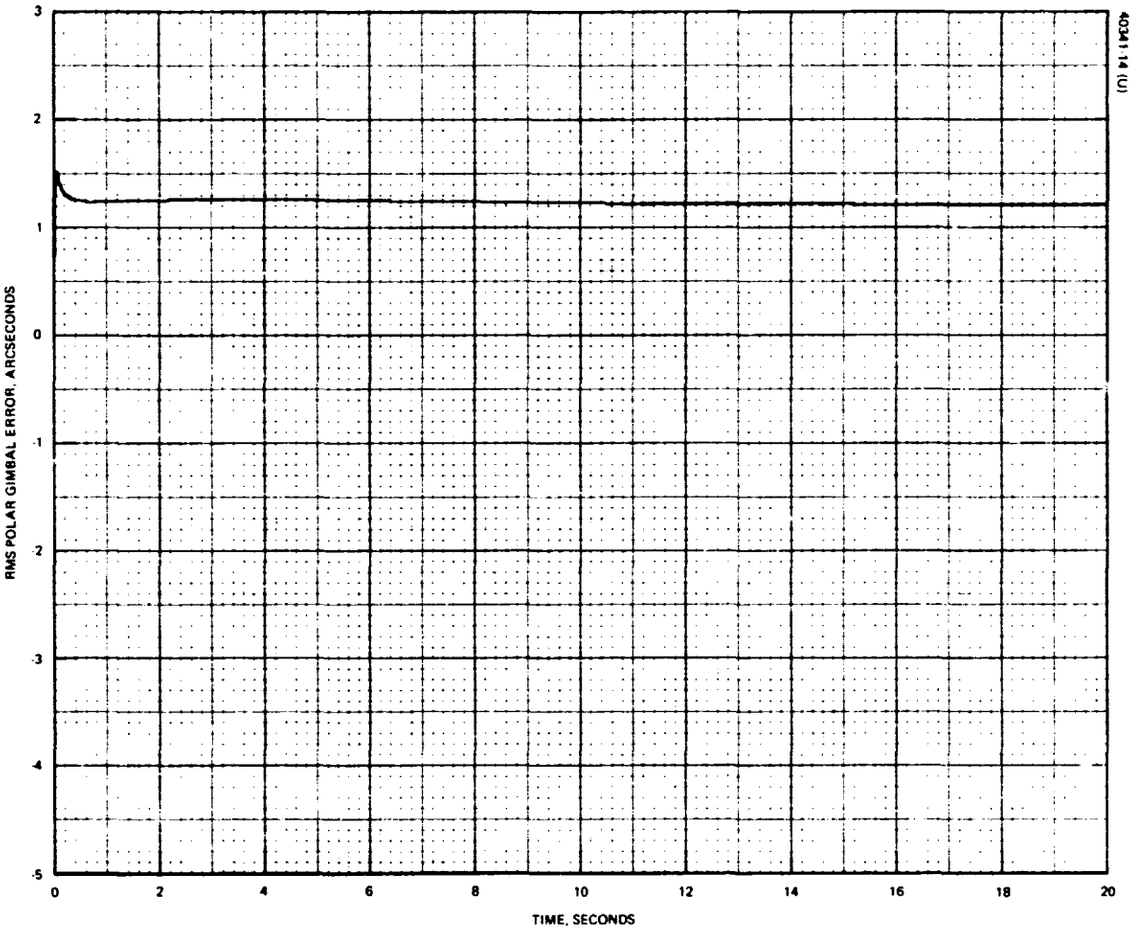

FIGURE 4-8. RMS POLAR GIMBAL ERROR

4.2 Control System

Figure 4-9 shows the control system configuration block diagram. The command to the control system is the desired spacecraft attitude. The spacecraft pointing error, which is obtained by comparing the reference attitude to the actual spacecraft attitude measured by STARS, is passed through a shaping network that commands a torquer to torque the spacecraft in order to produce the required attitude correction. This system contains two major disturbance sources; the spacecraft disturbance torques and the sensor noise on the STARS measurement of spacecraft attitude. The shaping network is designed to attenuate the STARS sensor noise and compensate for the disturbance torques.

The control system of Figure 4-9 was simulated under the assumptions that the torquer is ideal (no dynamics) and that STARS gives a perfect measurement of the spacecraft attitude. The purpose of this simulation was to investigate the system's ability to control the spacecraft dynamics and compensate for the disturbance torques.

Figures 4-10 thru 4-12 show the control system response when no disturbances are acting on the system. Figure 4-10 shows the spacecraft attitude over one orbit to be perfect. Figures 4-11 and 4-12 show the spacecraft's body rates. From the definition of the coordinate systems (see Figure 4-13), the body rates for perfect pointing should be:

$$\omega_{yaw} = \dot{\beta} \sin\gamma \sin\alpha = .04 \sin \dot{\alpha} t \ \frac{\text{arcsecond}}{\text{second}}$$

$$\omega_{roll} = \dot{\beta} \sin\gamma \cos\alpha = .04 \cos \dot{\alpha} t \ \frac{\text{arcsecond}}{\text{second}}$$

$$\omega_{pitch} = \dot{\beta} \cos\gamma + \alpha = 206 \text{ arcsecond/second}$$

where $\dot{\alpha}$ = orbit rate

From examination of the three figures, it can be stated that under ideal conditions and no disturbances, the control system can point the spacecraft perfectly.

Figures 4-14 thru 4-16 show the control system response when disturbance torques are acting on the system. Figure 4-14 shows the spacecraft attitude time history for one orbit period. The large peak in the roll response is an initial transient due to the manner in which the simulation was initialized. The pointing error caused by the disturbance torque is well within the prescribed accuracy of STARS. Figures 4-15 and 4-16 show the spacecraft body rates. The body rates are seen to be unaffected by the disturbance torques.

It can be concluded from the above simulations that the control system design of Figure 4-9 can control the spacecraft dynamics and also compensate for any disturbance torques acting on the spacecraft.

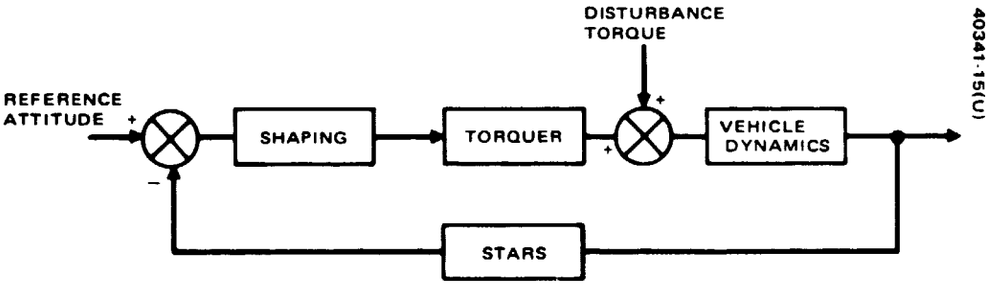

FIGURE 4-9. CONTROL SYSTEM CONFIGURATION

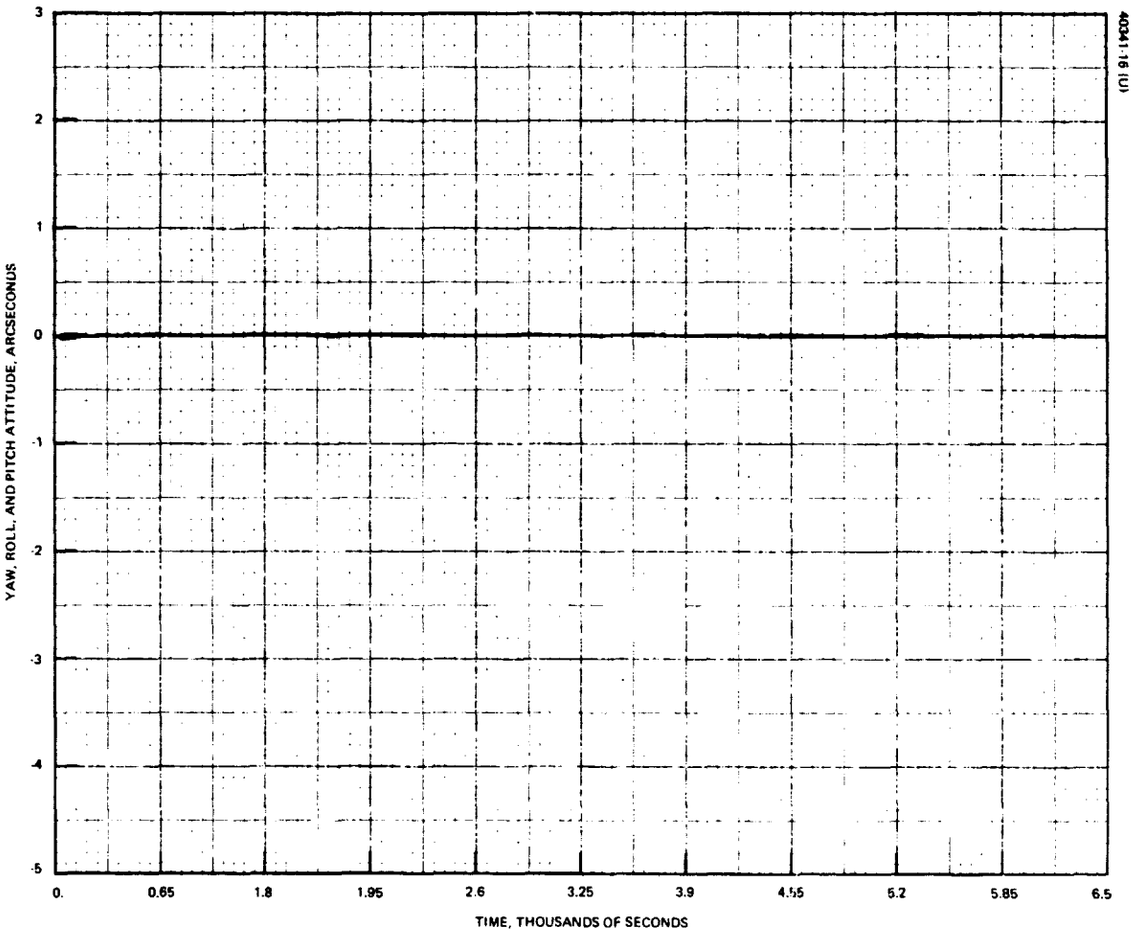

FIGURE 4-10. SPACECRAFT ATTITUDE, ZERO DISTURBANCE TORQUES

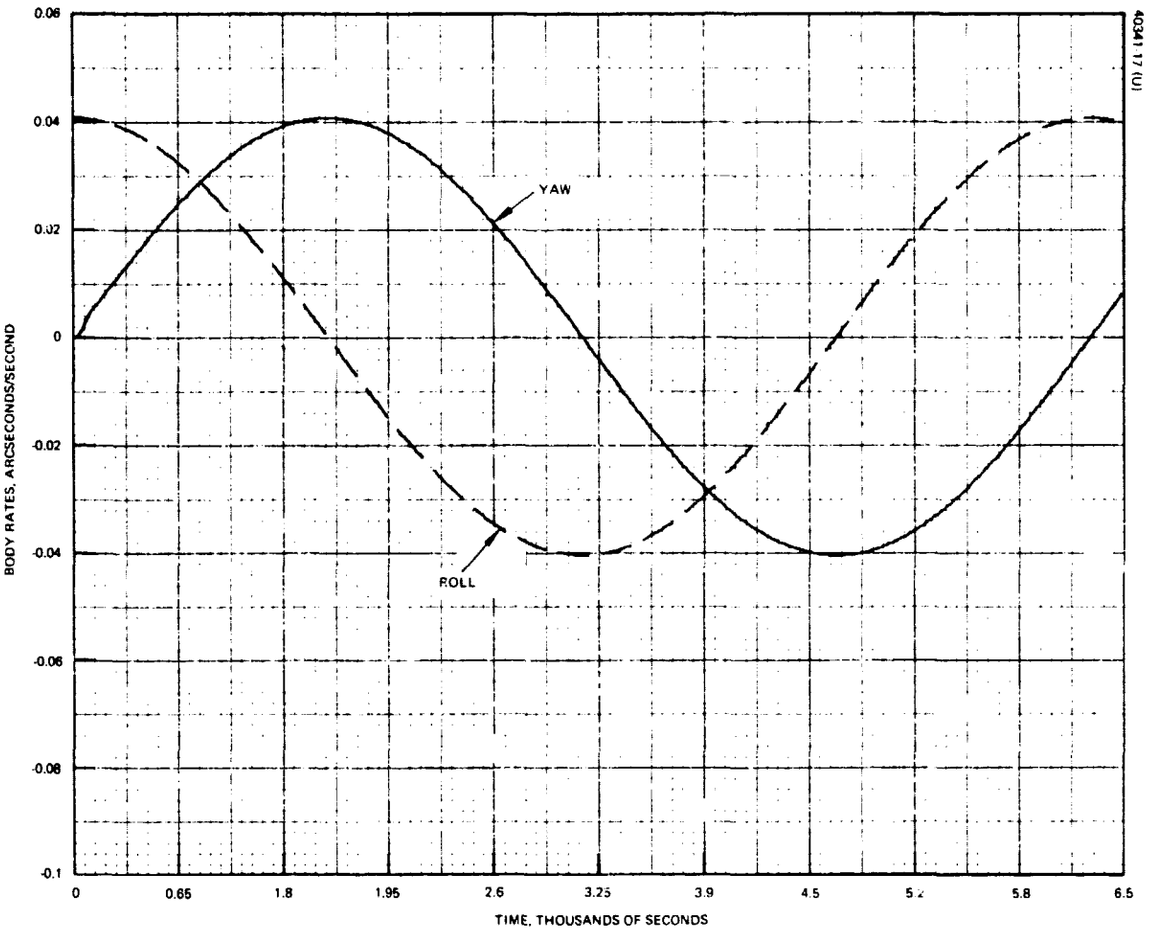

FIGURE 4-11. ROLL-YAW BODY RATES, ZERO DISTURBANCE TORQUES

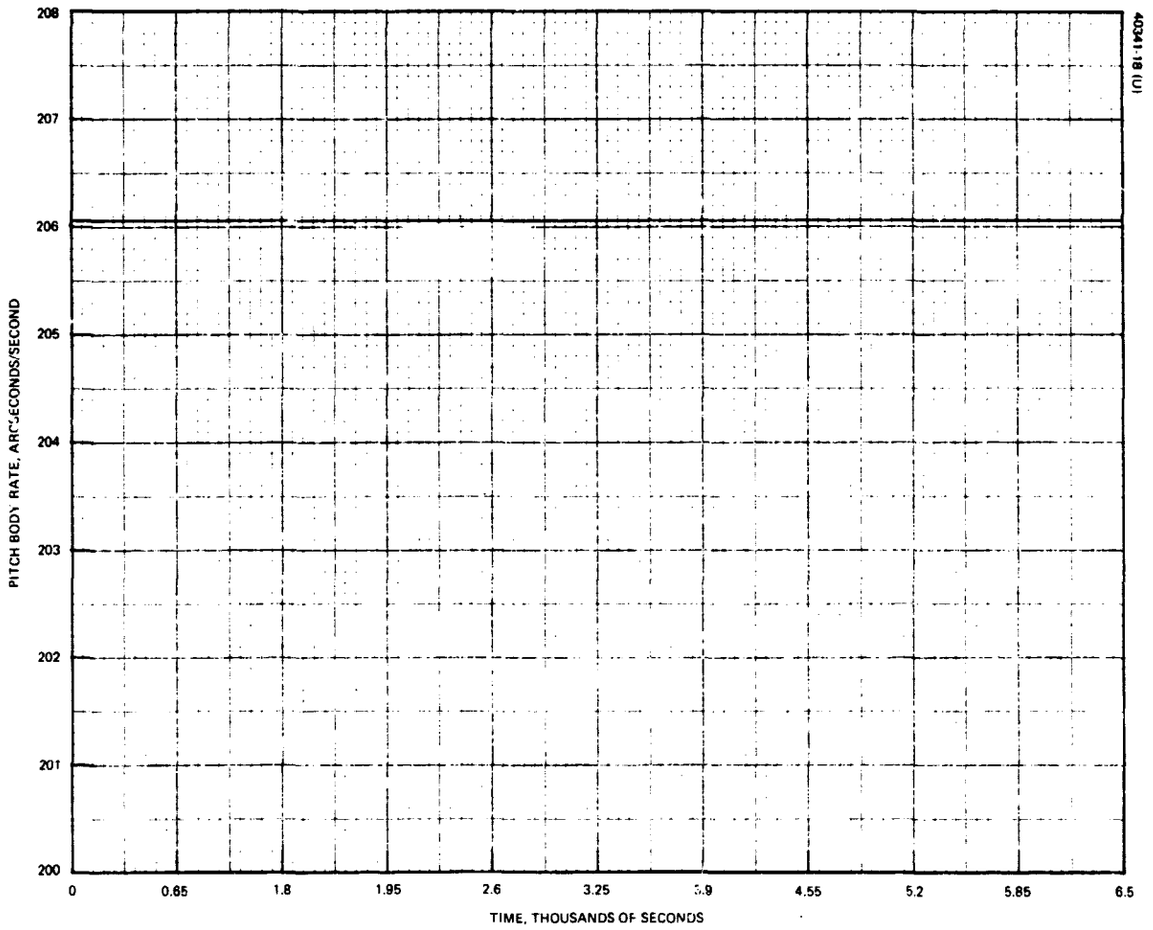

FIGURE 4-12. PITCH BODY RATE, ZERO DISTURBANCE TORQUES

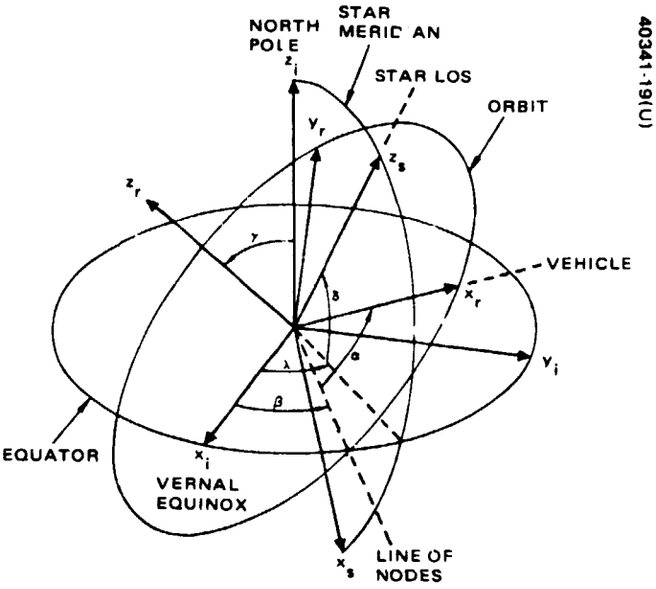

FIGURE 4-13. STARS GEOMETRY

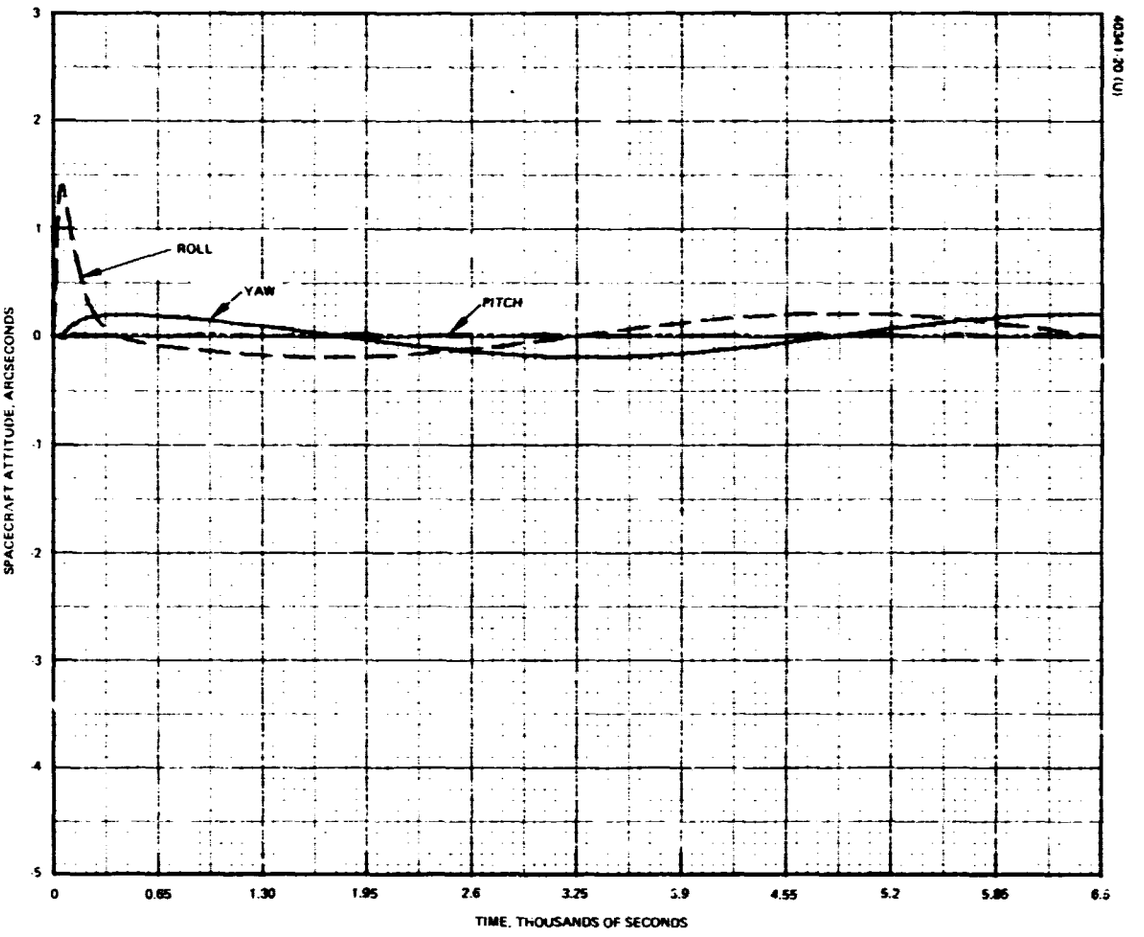

FIGURE 4-14. SPACECRAFT ATTITUDE, DISTURBANCE TORQUES PRESENT

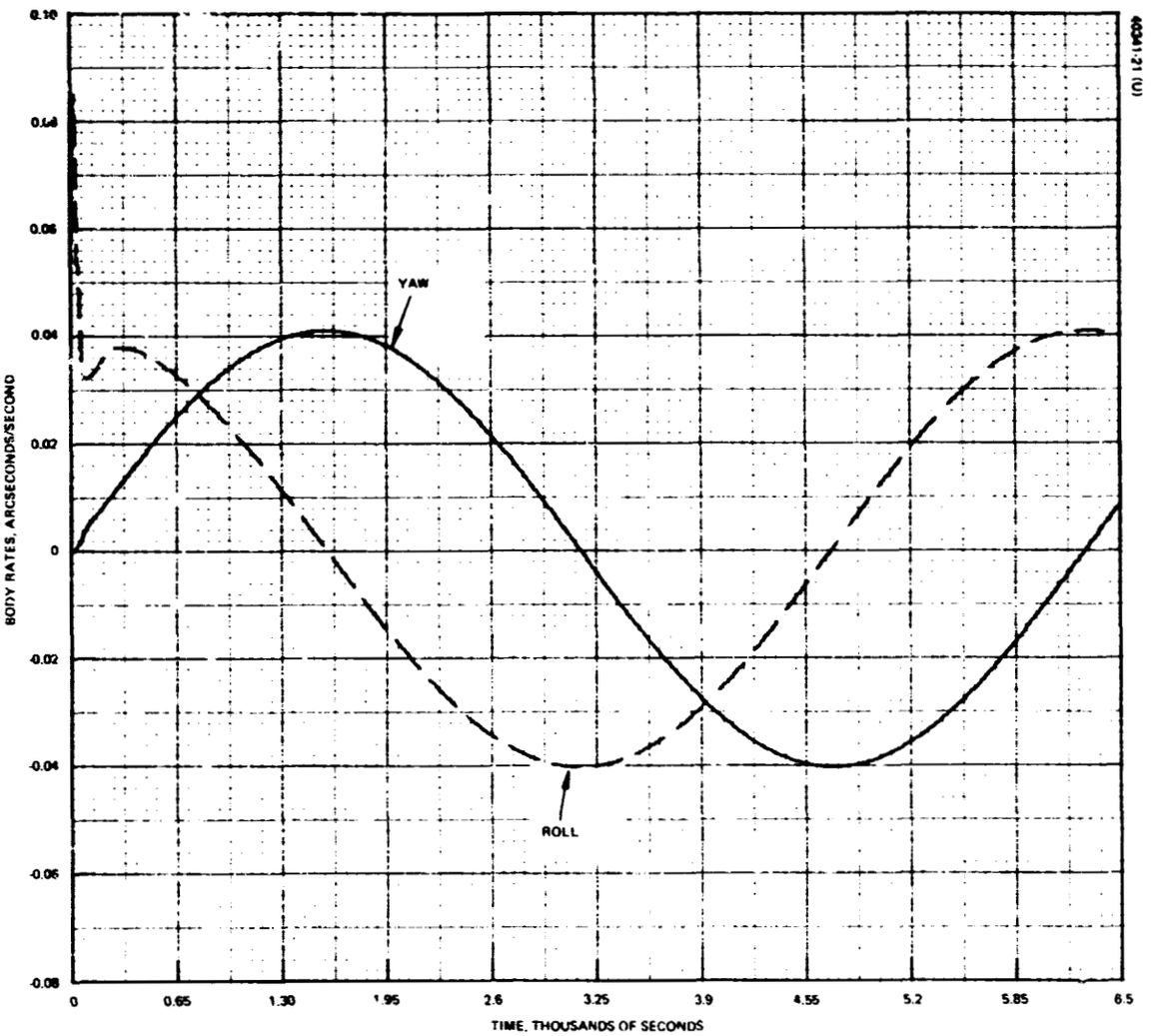

FIGURE 4-15. ROLL-YAW BODY RATES, DISTURBANCE TORQUES PRESENT

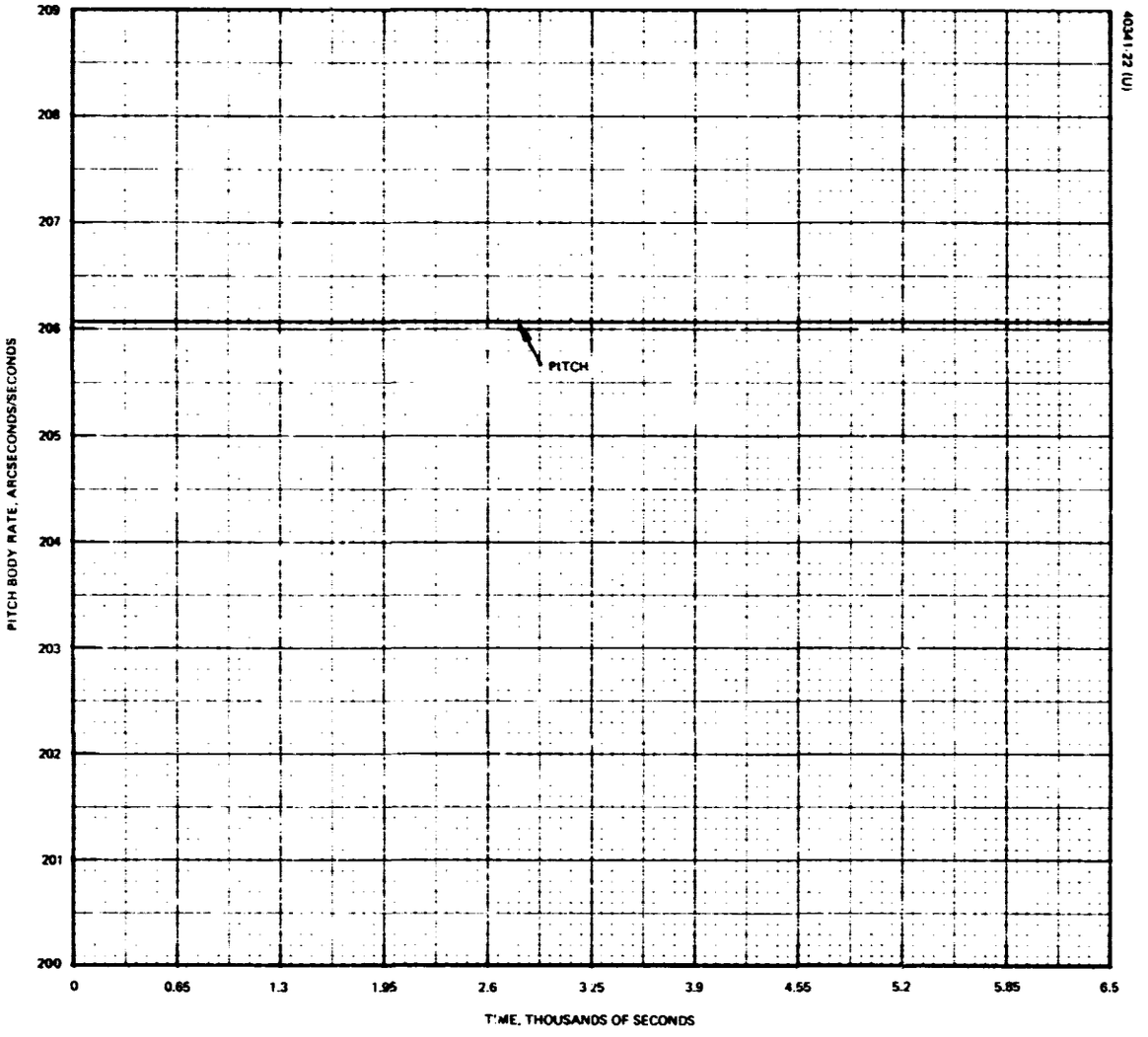

FIGURE 4-16. PITCH BODY RATE, DISTURBANCE TORQUES PRESENT

4.3 Star Tracker

A block diagram of the tracker model illustrating the relationships of its component functions is shown in Figure 4-17.

The time interval (Δt) between a position reference pulse coming from a pickoff on the optical wedge and the pulse produced by the star image crossing the recticle slit within the telescope is stored in a register for use by the tracker system. The register is updated every 250 milliseconds. A sinusoidal relation exists between the time interval and the corresponding error angle, given the scan circle radius and its period. Thus, the star line-of-sight error angle is derived directly from the pulse time interval measurement.

The realistic tracker model includes inputs for the two major disturbances to the system; missed (or false) pulses and pulse jitter. Both photon noise from the star background and dark current noise of the photomultiplier tube will cause missed (or false) pulses. This subject was treated in Section 2 of this report. With respect to this type of disturbance, the following assumptions were made in conjunction with the simulation model:

1) Missed or false pulses will perturb the system in the same manner.

2) An exponential noise distribution is assumed, yielding the worst case condition of 72 missed and 75 false pulses per hour.

3) By the use of electronic gating, detection of missed and false pulses will be possible.

4) If a missed (or false) pulse occurs on one of the star signals, the system will ignore that signal and use the last stored value of error corresponding to this signal.

Resolution of a pulse in time (pulse jitter) and hence the angular error associated with detection of the signal depends directly on pulse (or slit) width and inversely on signal-to-noise ratio. Using the baseline star tracker parameter

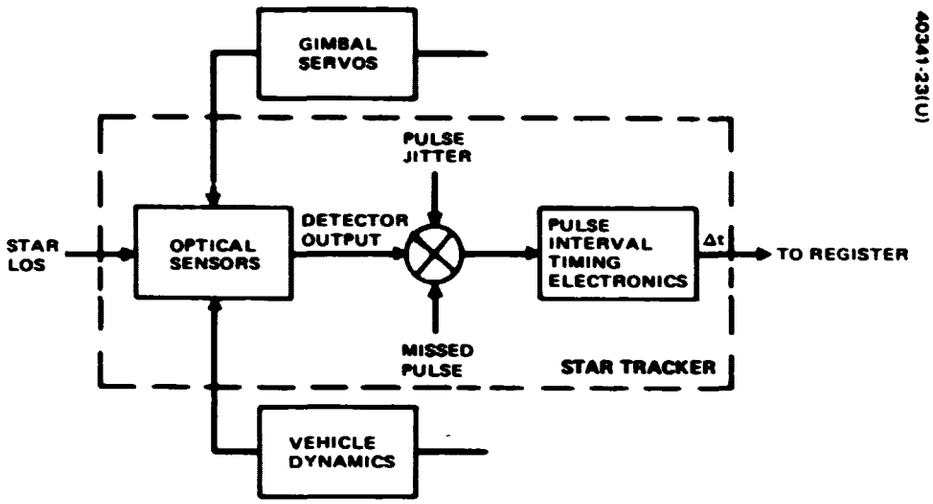

FIGURE 4-17. STAR TRACKER CONFIGURATION

values given in the STARS Feasibility Study, the 1σ value of track loop angle noise (pulse jitter) is 1.15 arcseconds.

Figures 4-18 thru 4-21 show the STARS system response when the star tracker simulation model is added to the control system simulation of Section 4.2. In this case, no disturbance torques are acting on the spacecraft and the torquer is still ideal. Figure 4-18 shows the spacecraft attitude time history for half an orbit period. A peak to peak error of approximately .20 arcsecond is observed in all three axes. This is obviously well within the accuracy requirements of the STARS system. Figure 4-19 shows the star tracker's estimate of the spacecraft pointing error. If the estimate were perfect Figure 4-18 and 4-19 would be identical. However, by a comparison, the measurement is seen to be very noisy, yet the spacecraft error is very small. The important point demonstrated here is that the error in the star tracker's estimate is filtered by the large inertia of the vehicle. Figures 4-20 and 4-21 show the body rates. These rates contain a small magnitude, high frequency component in addition to the required perfect pointing rates.

In conclusion, this simulation shows that the present star tracker design will provide the required high accuracy performance.

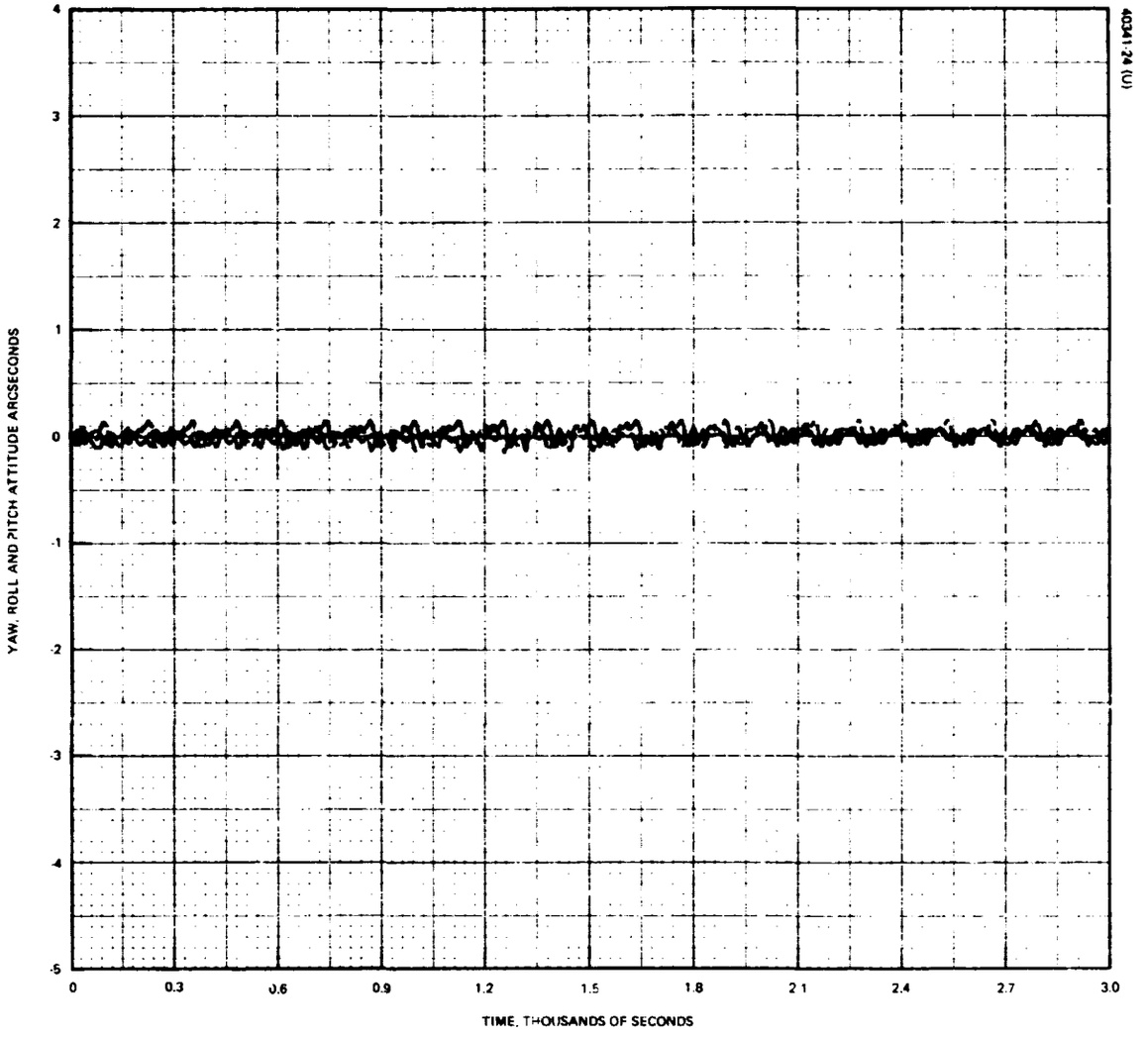

FIGURE 4-18. SPACECRAFT ATTITUDE WITH TYPICAL STAR TRACKER NOISE BUT NO DISTURBANCE TORQUES

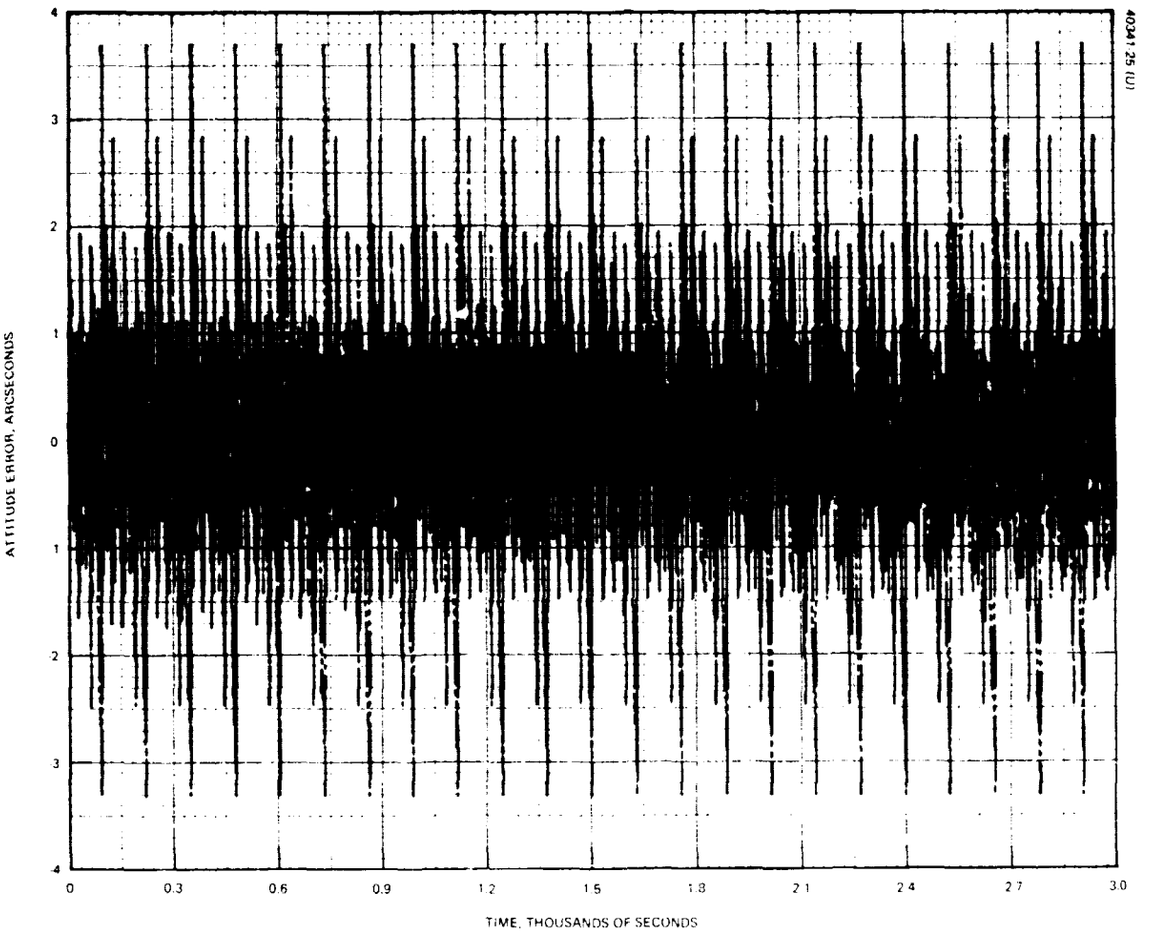

FIGURE 4-19. STAR TRACKER ESTIMATE OF POINTING ERROR, ZERO DISTURBANCE TORQUES

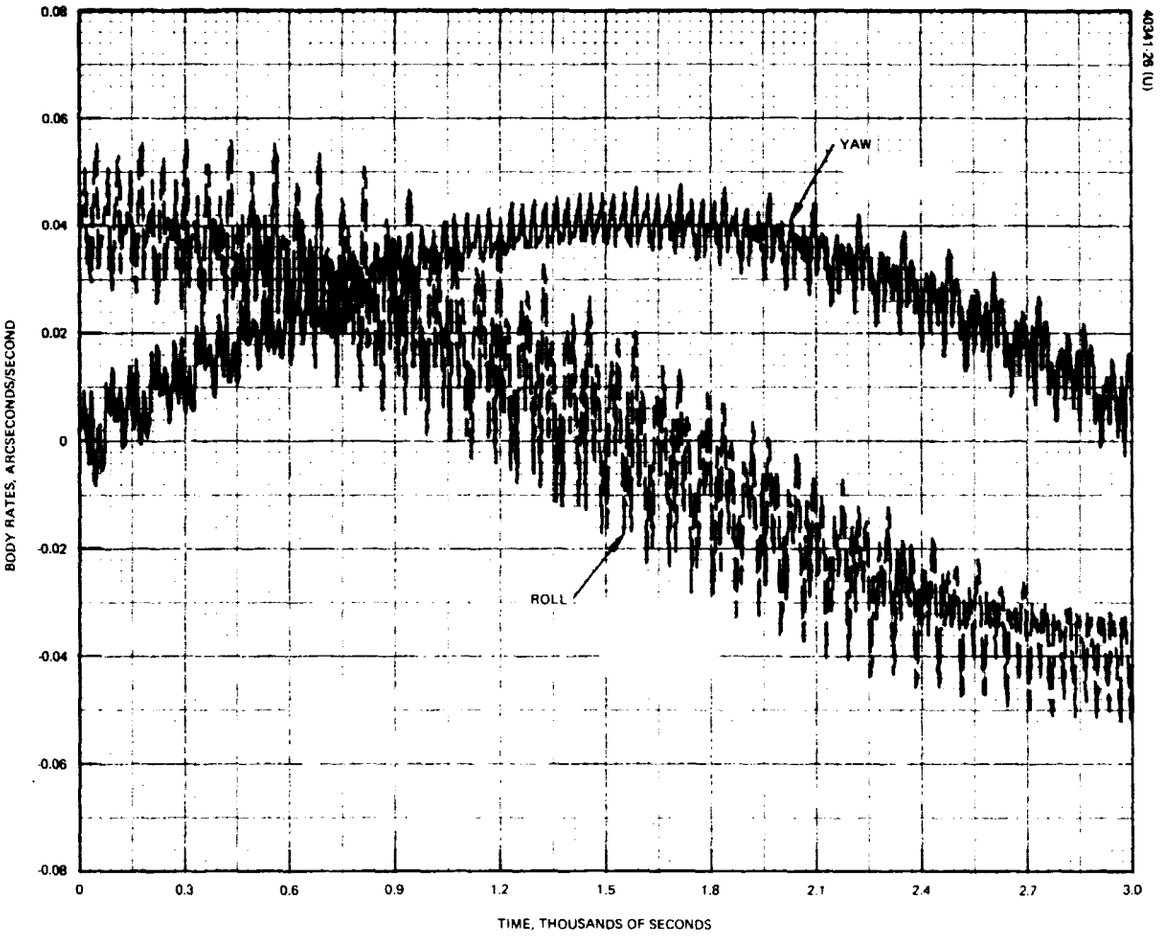

FIGURE 4-20. ROLL-YAW BODY RATES WITH TYPICAL STAR TRACKER NOISE BUT NO DISTURBANCE TORQUES

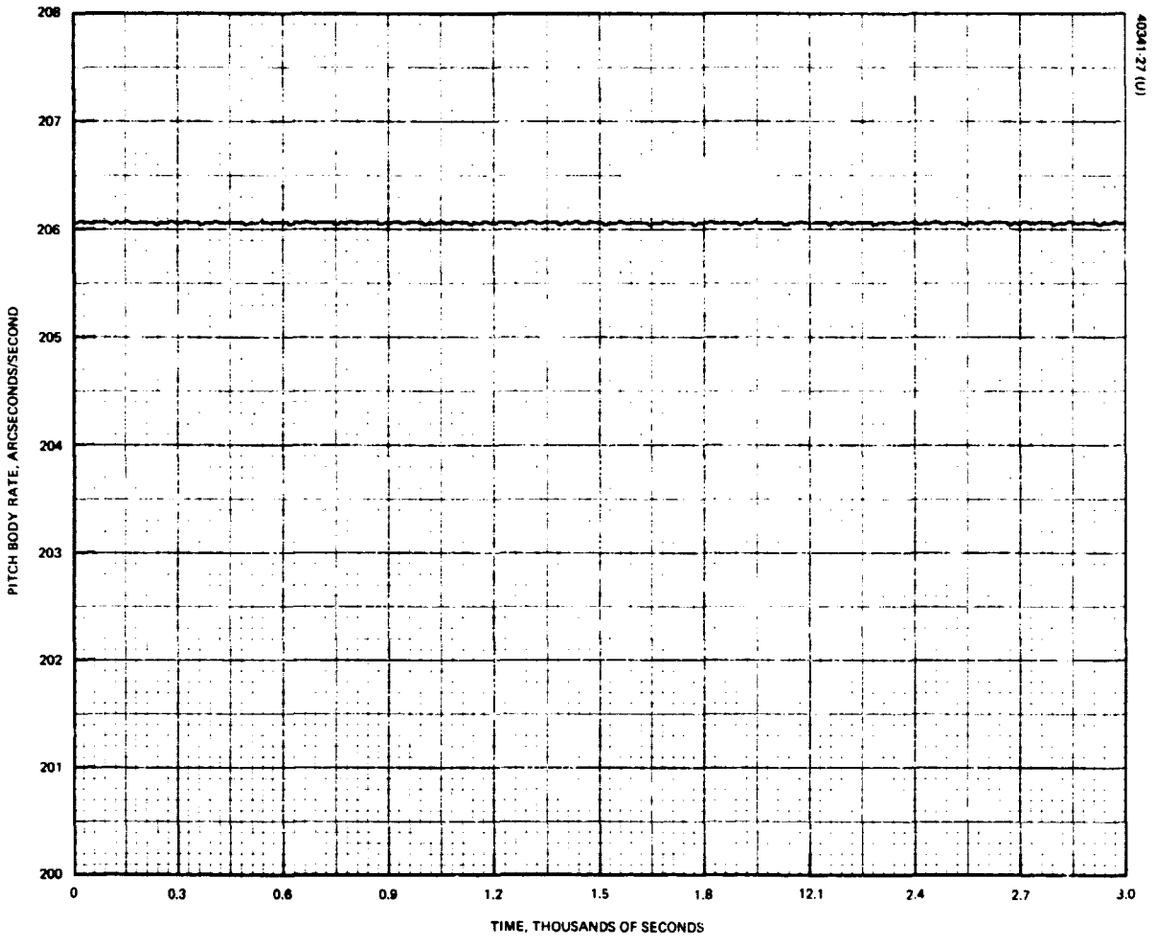

FIGURE 4-21. PITCH BODY RATE WITH TYPICAL STAR TRACKER NOISE BUT NO DISTURBANCE TORQUES

4.4 STARS System Model

A signal flow diagram of the complete STARS system, illustrating the functional interfaces between the computer, telescope assembly, and the spacecraft attitude control system is shown in Figure 4-22. The functional description of the individual components of the system have been discussed previously.

The total system was simulated on a GE635 digital computer using the MIMIC simulation language. The computer simulation flow diagram is given in Figure 4-23. The complete STARS system simulation is a combination of the simulation models of the precision gimbals, the star tracker, and the control system discussed previously, with some additional modelling added for the on-board computer requirements. All major disturbances were included. The computer listing can be found in Appendix 5.2.

Figures 4-24 through 4-27 show the complete STARS system response for one orbit period. The spacecraft attitude is shown in Figure 4-24. The response consists of an error component at orbit frequency due to the disturbance torques and a high frequency error component due to the star tracker's estimate of spacecraft attitude. The maximum peak to peak error in spacecraft pointing is observed to be well less than half of an arcsecond. The star tracker's estimate of the spacecraft attitude is shown in Figure 4-25. By comparing this figure to 4-25, the filtering effect of the large mass of the spacecraft is observed once again. Figures 4-26 and 4-27 show the spacecraft body rates. These rates contain a small magnitude, high frequency component, due to STARS sensor noise, in addition to the required perfect pointing rates. This simulation shows convincingly that the STARS system has the ability of high precision spacecraft pointing.

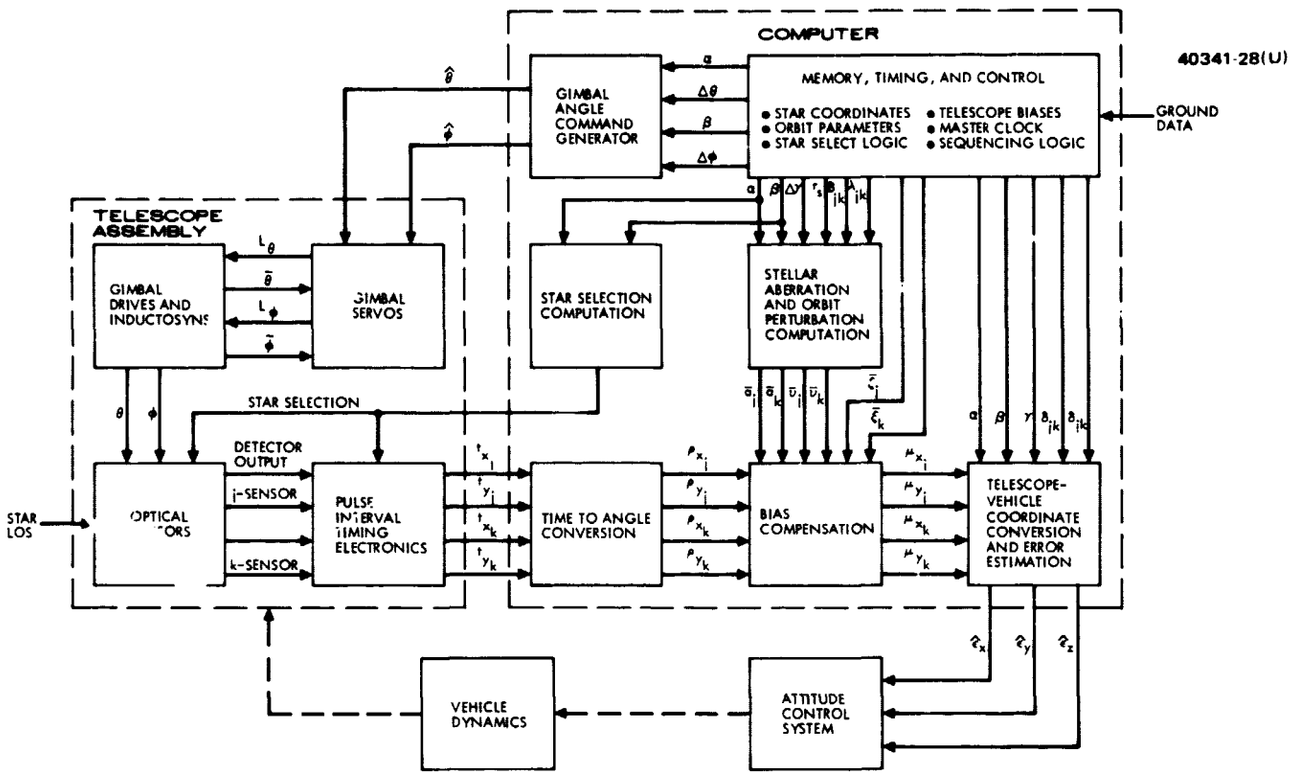

FIGURE 4-22. STARS SIGNAL FLOW DIAGRAM

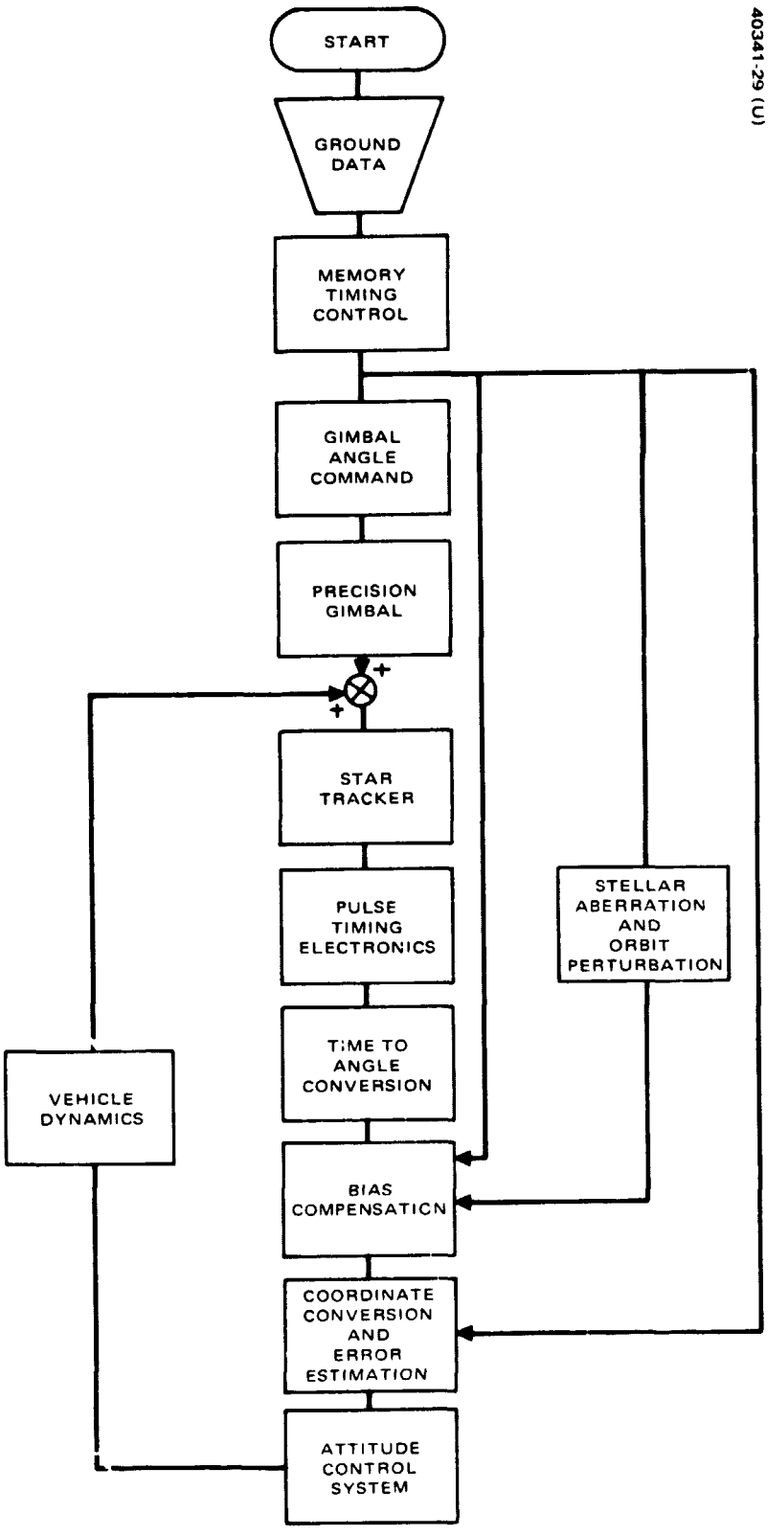

FIGURE 4-23. COMPUTER FLOW DIAGRAM

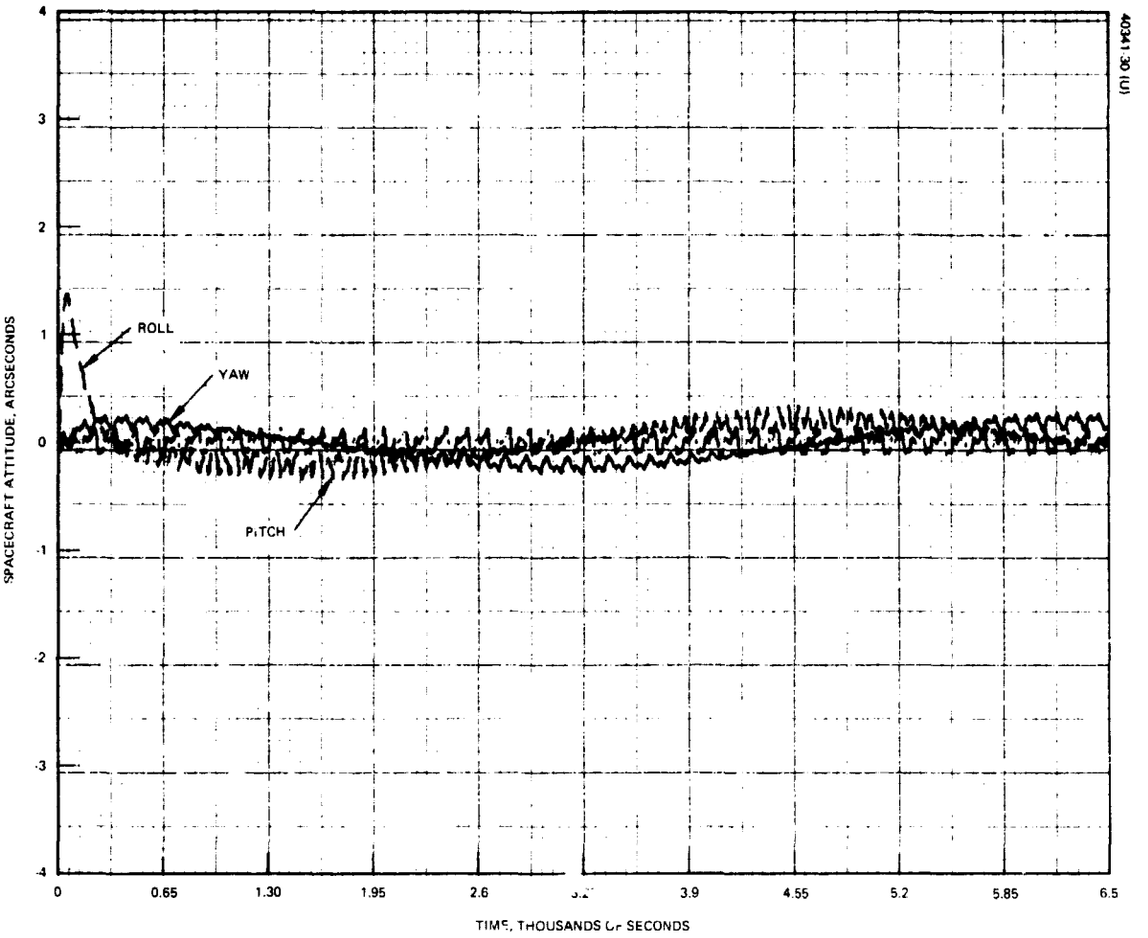

FIGURE 4-24. SPACECRAFT ATTITUDE, DISTURBANCE TORQUES AND STAR TRACKER NOISE INCLUDED

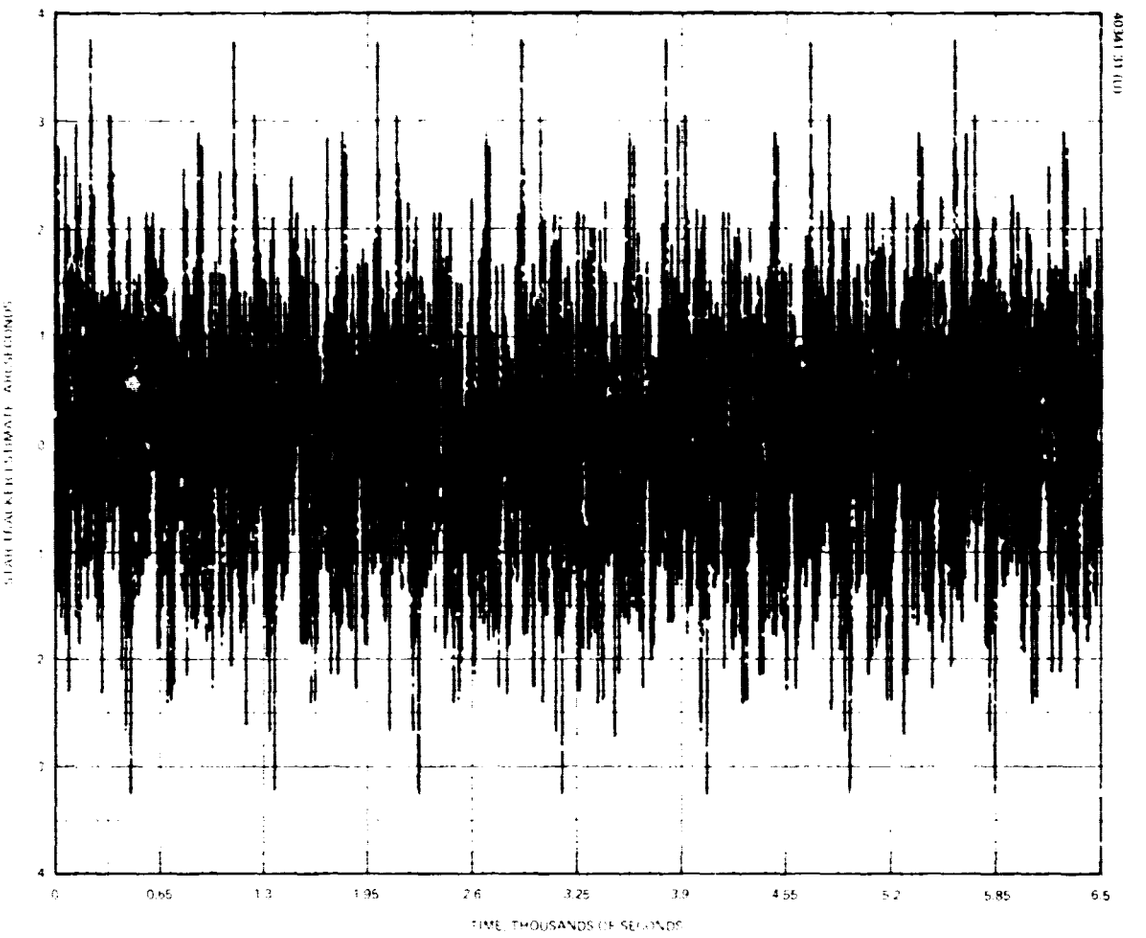

FIGURE 4-25. STAR TRACKER ESTIMATE OF POINTING ERROR, DISTURBANCE TORQUES INCLUDED

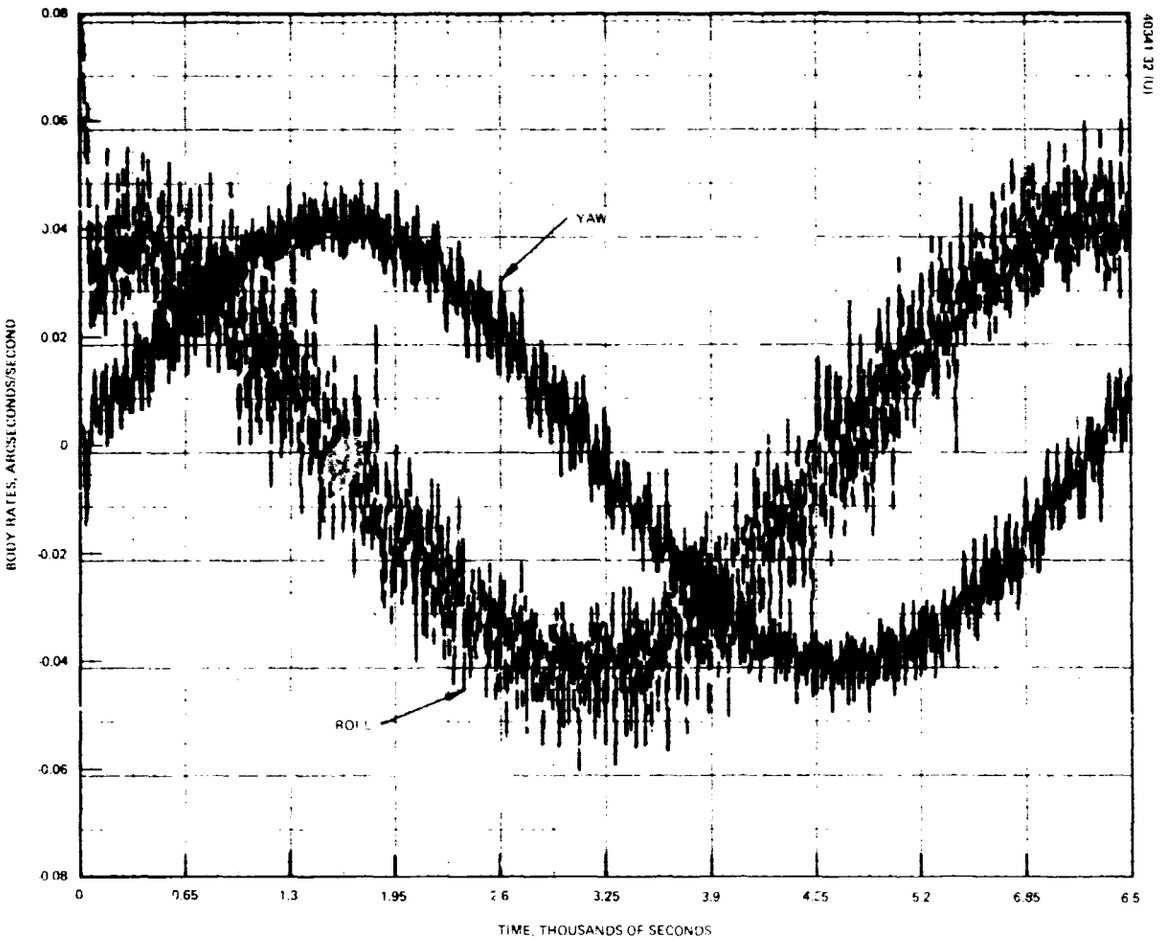

FIGURE 4-26. ROLL-YAW BODY RATES, DISTURBANCE TORQUES AND STAR TRACKER NOISE INCLUDED

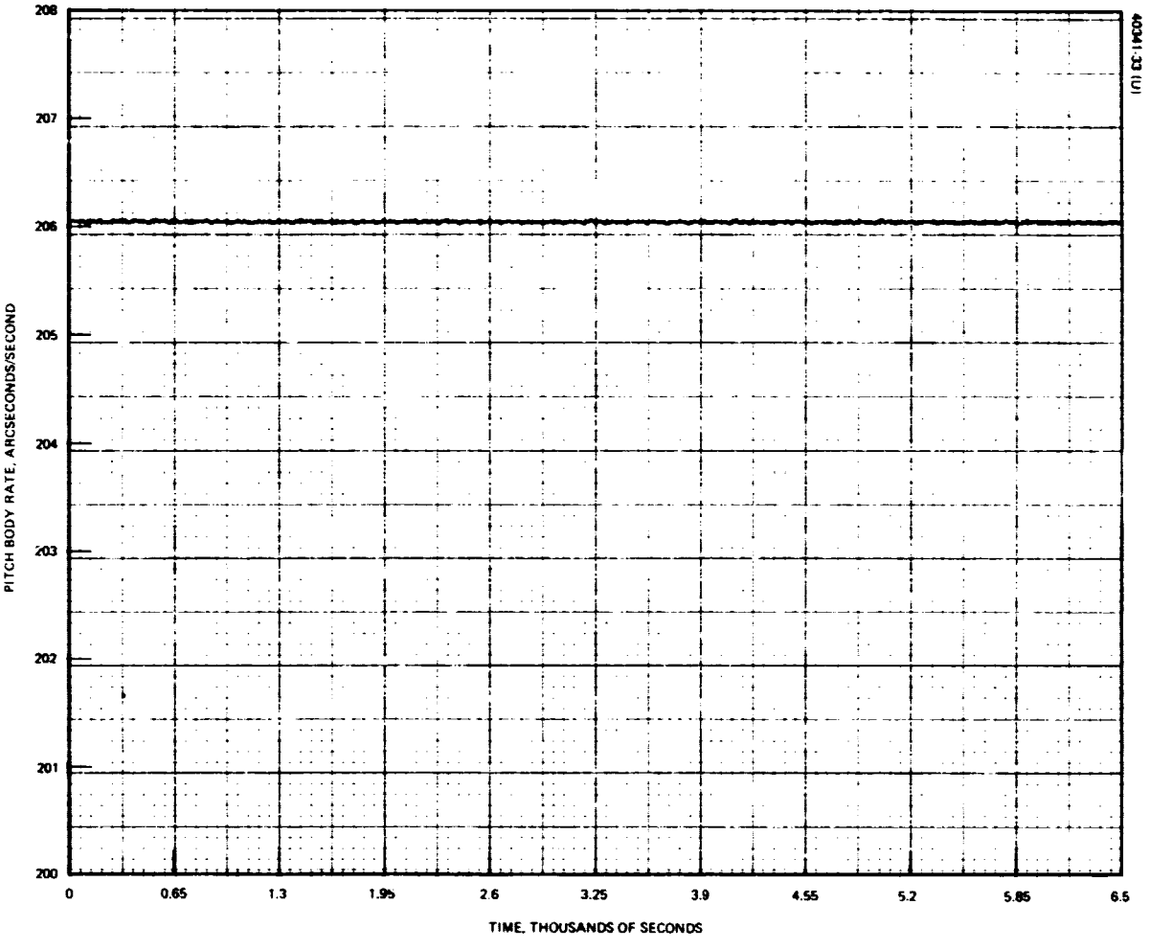

FIGURE 4-27. PITCH BODY RATE, DISTURBANCE TORQUES AND STAR TRACKER NOISE INCLUDED

Three additional runs were made using the complete STARS system simulation to investigate the effect of gimbal axis misalignment, the effect of a non-ideal torquer, and the initial acquisition ability of STARS.

1) Gimbal axis misalignment

The effect of an error in the built-in angle between the pitch and polar axis of the telescope assembly was considered. A three arcsecond error in this angle was assumed to be representative of this type of an error. The total STARS system simulation described above was run with this three arcsecond gimbal misalignment. The system response to this error was not visible, thus yielding a conclusion that this type of error will not affect the STARS system performance.

2) Non-ideal Torquer

A one second deadband region was added to the torquer model shown in Figure 4-9. The system response to this error is very small. Figure 4-28 shows the spacecraft attitude for this simulation run. When comparing this figure with Figure 4-24, an increase in the peak to peak magnitude of the pointing error of .1 arcsecond is observed. This type of error has a greater effect on spacecraft pointing than the gimbal misalignment error, however even with this error, the STARS control system is well within its accuracy requirements.

3) Initial Acquisition

The acquisition problem of the STARS system begins when the star's image is first seen in the telescope. The image will first appear when the error between the telescope boresight axis and the line-of-sight to the star is less than .5 degrees (1800 arcseconds).

This condition was simulated by giving the spacecraft an appropriate initial attitude so that the error in the telescope frame was approximately .5 degrees. The STARS system response for this simulation is shown in Figures 4-29 through 4-31. Figure 4-29 shows that the spacecraft pointing error is brought to zero in approximately 300 seconds. Figures 4-30 and 4-31 show the spac_craft's body rates, which are also brought to their respective perfect pointing values in approximately 300 seconds.

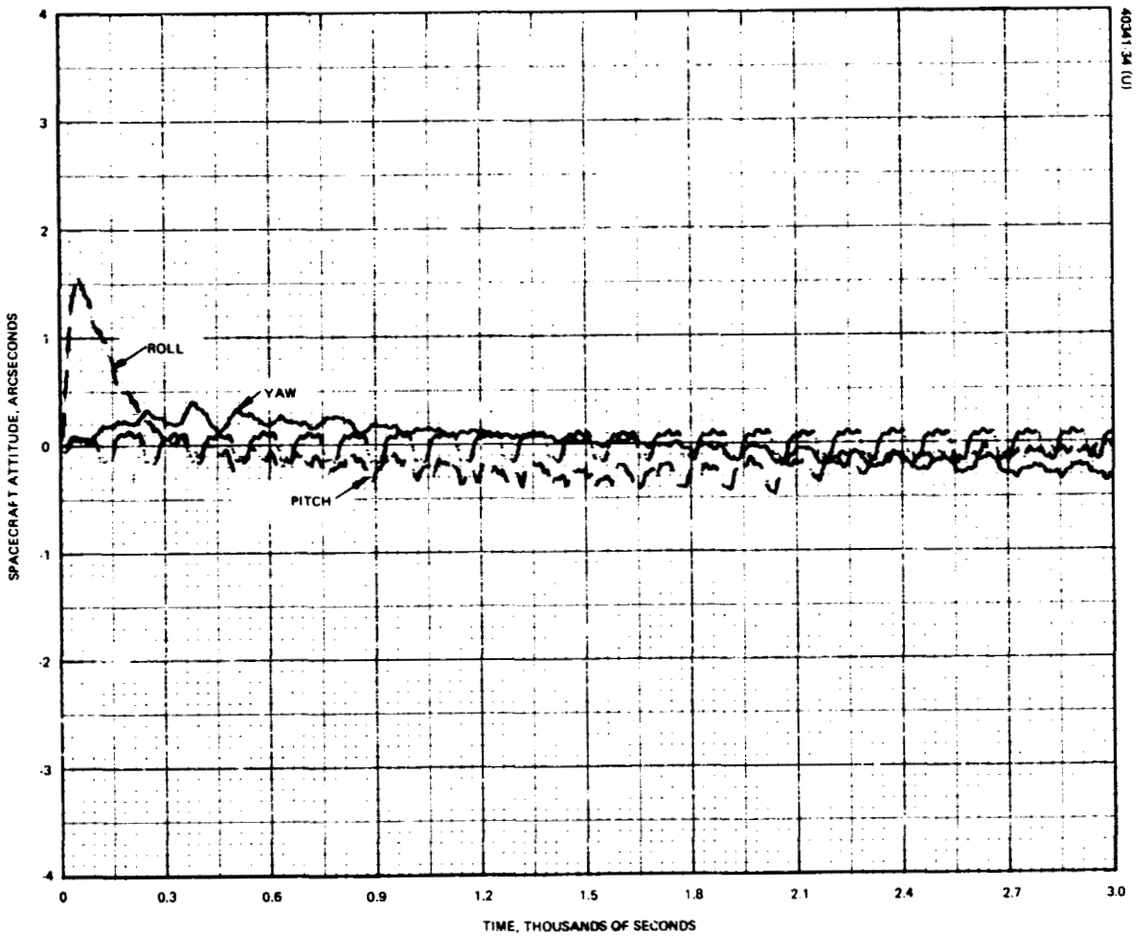

FIGURE 4-28. SPACECRAFT ATTITUDE USING CONTROL TORQUER WITH DEADBAND

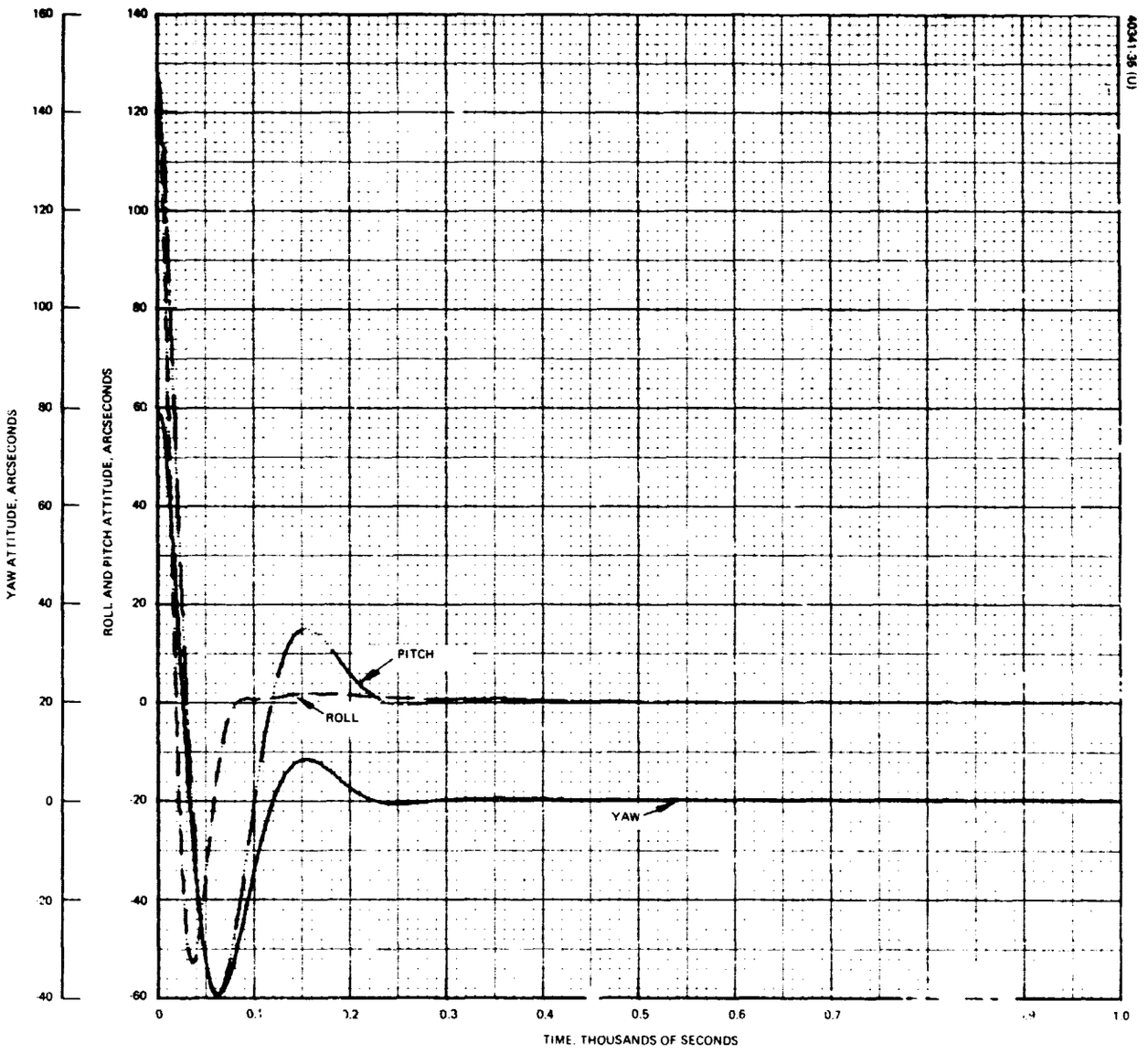

FIGURE 4-29. SPACECRAFT ATTITUDE, INITIAL ACQUISITION

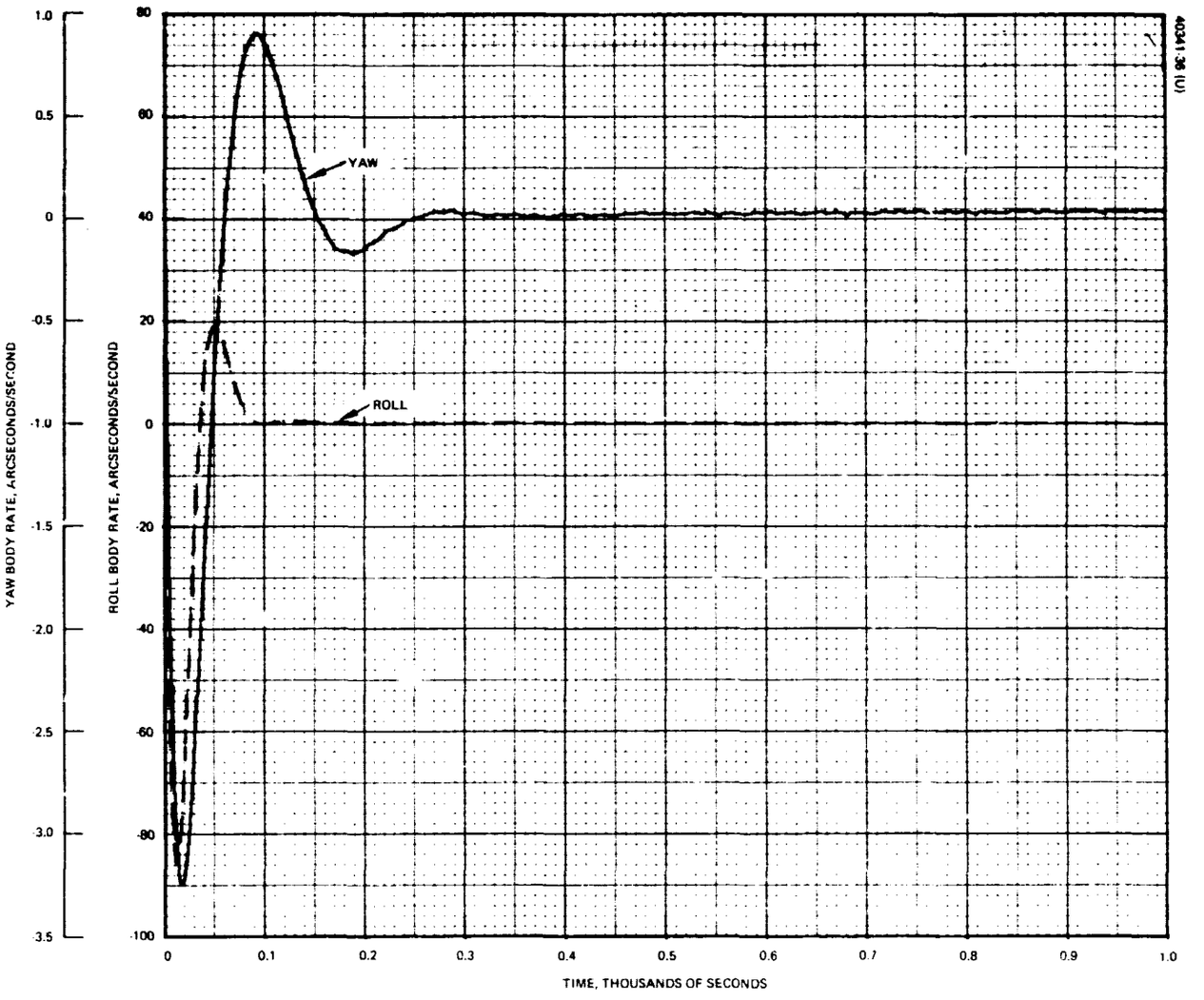

FIGURE 4-30. ROLL-YAW BODY RATES, INITIAL ACQUISITION

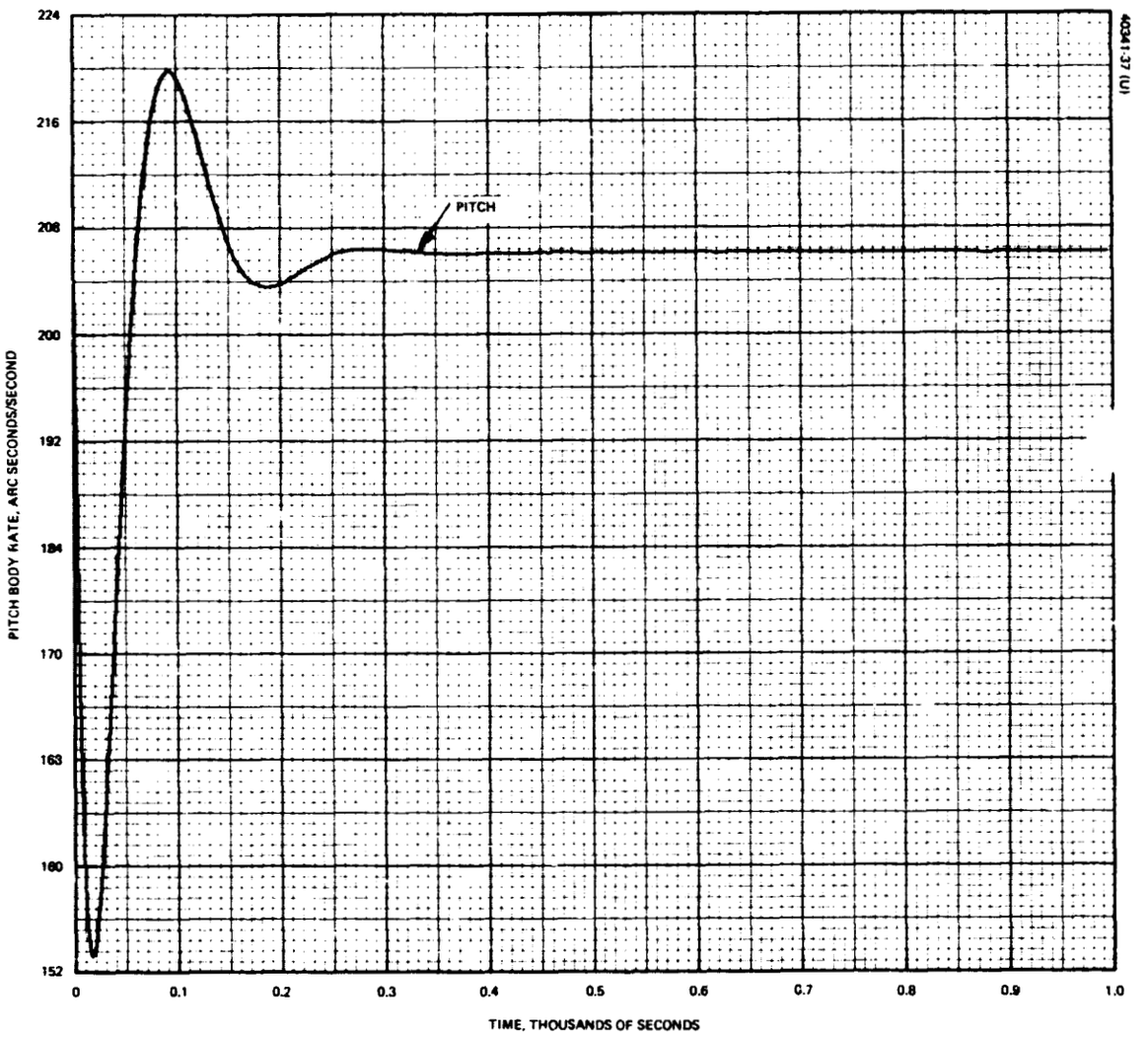

FIGURE 4-31. PITCH BODY RATE, INITIAL ACQUISITION

4.5 Conclusions

A number of conclusions may be reached, based on the analyses, experiments, and simulations performed in this study. These cover star tracker characteristics and performance, the capabilities of the precision gimbal system, control loop design, acquisition performance, pointing precision and pointing stability.

Star tracker analyses, based on experimental data from several photomultiplier tubes, indicate that without using elaborate electronic processing, the false alarm and missed pulse rate to be anticipated lies between 75 per hour and 4 per hour. Even though these rates appear quite acceptable, an additional order of magnitude improvement is available if needed by applying time gating of the star pulses as part of the signal processing.

A detailed simulation of STARS gimbal characteristics shows that the gimbals may be positioned with a precision of better than two arcseconds, using shaft angle transducers with a resolution of 19 bits. Since the gimbal positioning precision appears to be limited chiefly by the resolution of the feedback transducer, the prospects of higher pecision in this area (if desired) are very good.

Simulation of the spacecraft control system shows that a relatively uncomplicated control system design can reduce the effect of various external disturbance torques on pointing precision to negligible values while simultaneously keeping pointing jitter due tosensor noise at acceptable levels. It was found that a pointing error of 0.5 arcsecond due to disturbance torques and less than 0.2 arcsecond jitter due to sensor noise is achievable without placing significant demands on system gains or bandwidth. At the same time the transient response of the overall system appears quite adquate, with acquisition from the edge of the field of view occurring in less than 300 seconds:

The overall conclusion that may be drawn from the results of the STARS

System Application Study is that a relatively straightforward precision pointing system design utilizing STARS on an EOS type spacecraft, and considering the characteristics of real sensing and control hardware, can achieve the desired 0.001 degree earth pointing capability. The STARS approach should therefore be a strong contender in any application where a large payload must be pointed earthward with high precision from any arbitrary orbit.

5. APPENDIX

5.1 Spacecraft Equations of Motion

The spacecraft angular momentum is

$$\bar{H} = I\bar{\omega}$$

or, in expanded form

$$\begin{bmatrix} H_R \\ H_P \\ H_Y \end{bmatrix} = \begin{bmatrix} I_R & I_{RP} & I_{RY} \\ I_{PR} & I_P & I_{PY} \\ I_{YR} & I_{YP} & I_Y \end{bmatrix} \begin{bmatrix} \omega_R \\ \omega_P \\ \omega_Y \end{bmatrix}$$

For the EOS configuration specified by GSFC, the only non-zero crossproduct of inertia is I_{RY} (= I_{YR}). Therefore

$$\bar{H} = \begin{bmatrix} I_R\omega_R + I_{RY}\omega_Y \\ I_P\omega_P \\ I_Y\omega_Y + I_{RY}\omega_R \end{bmatrix}$$

and

$$\dot{\bar{H}} = \begin{bmatrix} I_R\dot{\omega}_R + I_{RY}\dot{\omega}_Y \\ I_P\dot{\omega}_P \\ I_Y\dot{\omega}_Y + I_{RY}\dot{\omega}_R \end{bmatrix}$$

The moment equation is

$$\bar{M} = \dot{\bar{H}} + \bar{\omega} \times \bar{H}$$

now,

$$\bar{\omega} \times \bar{H} = \begin{bmatrix} i & j & k \\ \omega_R & \omega_P & \omega_Y \\ H_R & H_P & H_Y \end{bmatrix}$$

$$\begin{bmatrix} H_Y\omega_P - H_P\omega_Y \\ -H_Y\omega_R + H_R\omega_Y \\ H_P\omega_R - H_R\omega_P \end{bmatrix}$$

Thus the expanded moment equations are

$$M_R = I_R\dot{\omega}_R + I_{RY}\dot{\omega}_Y + I_{RY}\,\omega_P\,\omega_R + I_Y\,\omega_P\,\omega_Y - I_P\,\omega_P\,\omega_Y$$

$$M_P = I_P\dot{\omega}_P - I_{RY}\,\omega_R^2 - I_Y\,\omega_R\,\omega_Y + I_R\,\omega_R\,\omega_Y + I_{RY}\,\omega_Y^2$$

$$M_Y = I_Y\,\dot{\omega}_Y + I_{RY}\,\dot{\omega}_R + I_P\,\omega_R\,\omega_P - I_R\,\omega_R\,\omega_P - I_{RY}\,\omega_p\,\omega_Y$$

5.2 COMPUTER PROGRAM LISTINGS

```
$       IDENT   366,54790,1087D,78294,ROY
$       LIMITS  30,30K,,10K,,1
$       PROGRAM RLHS,NDUMP
$       LIMITS  30,30000,,10000
$       PERM    H*,MIMIC-SYSTEM
$       TAPE    09,A2S
                CON(K1,KM1,KI1,KD1)
                CON(TAU1,TAU11,R1,J1)
                CON(THETD0,THETA0)
                DBM(TRUE)
        DTMIN   1/(2**13)
        DTMAX   DTMIN
        DT      .01
                FAM(T,20)
        SW1     FSW(T,FALSE,TRUE,FALSE)
SW1     KRDA    3600*180/3.14159
SW1     KS2     (KD1*K1*KM1)/R1
SW1     OMEG    (13.737*360)/24
        SW3     FSW(REM(T,.0015),FALSE,TRUE,FALSE)
SW3     ALPHA   OMEG*T
SW3     THECOM  ALPHA
SW3     THETAC  ING(KI1*THECOM)
        INDTER  RNG(0,1.75,.1)
        BEARER  RNG(0,1.137,.2)
        EI10    THETAC-THETB
        EI1     KS2*EI10
        P21     INT(EI1,0)
        P11     INT((10*TAU1+TAU11)*EI1-EO1+P21,0)
        EO1     (10*TAU1*TAU11*EI1+P11)/TAU1
        OI1     (EO1+F1)/J1
        F1      FSW(THETAD,.026,0,-.026)
        THETAD  INT(OI1,THETD0)
        THETA   INT(THETAD,THETA0)
        THETAA  KRDA*THETA+BEARER
        THETB   ING(KI1*(THETAA+INDTER))
        THEDEL  THECOM-THETAA
        R       (1/T)*INT(THEDEL,0)
        RMS     SQR((1/T)*INT(THEDEL*THEDEL,0)-R*R)
                PLO(T,RMS)
                SCL(20,0,5,-5)
                END
200         .376        .404        6.25E-3
.01         1           13          1.5
0           0
$       ENDJOB
```


PITCH GIMBAL SIMULATION

```
$       IDENT   366,54790,1087D,78294,ROY
$       LIMITS  10,30K,,10K,,1
$       PROGRAM RLHS,NDUMP
$       LIMITS  10,30000,,10000
$       PERM    H*,MIMIC-SYSTEM
$       TAPE    09,A2S
                   CON(KF2)
                   CON(PHID0,PHI0)
                   PAR(K2,KM2,KI2,KD2)
                   PAR(TAU2,TAU12,R2,J2)
                   PAR(COUNT,SUM)
                   DBM(TRUE)
          DTMIN    1/(2**5)
          DTMAX    DTMIN
          DT       1
                   FIN(T,1000)
          SW1      FSW(T,FALSE,TRUE,FALSE)
 SW1      KS       (KD2*K2*KM2)/R2
          SW3      FSW(REM(T,90),FALSE,TRUE,FALSE)
 SW1      KRDA     180*3600/3.14159
 SW1      OMEGA    360/(365.26*24)
 SW3      BETA     OMEGA*T
 SW3      PHICOM   BETA
 SW3      PHIC     ING(KI2*PHICOM)
          BEARER   RNG(0,1.137,.5)
          INDTER   RNG(0,1.75,.7)
********   ELASTIC STICTION MODEL
 SW3      CO       PHI
          SW4      FSW(ABS(PHID)-.000001,FALSE,TRUE,FALSE)
          SW5      COM(SW4)
 SW4      F2       0
 SW5      C1       PHI-CO
 SW5      F2       -KF2*C1
*******
          EI20     PHIC-PHB
          EI2      KS*EI20
          P22      INT(EI2,0)
          P12      INT((10*TAU2+TAU12)*EI2-EO2+P22,0)
          EO2      (10*TAU2*TAU12*EI2+P12)/TAU2
          OI2      (EO2+F2)/J2
          PHID     INT(OI2,PHID0)
          PHI      INT(PHID,PHI0)
          PHA      KRDA*PHI+BEARER
          PHB      ING(KI2*(PHA+INDTER))
          PHIDEL   PHICOM-PHA
          R1       (1/T)*INT(PHIDEL,0)
          RMS1     SQR((1/T)*INT(PHIDEL*PHIDEL,0)-R1*R1)
          PRINT    FSW(REM(T,10),FALSE,TRUE,FALSE)
 PRINT             OUT(T,PHA,PHICOM,PHIDEL,RMS1)
                   PLO(T,PHA,PHICOM)
                   SCL(1000,0,50,0)
                   PLO(T,PHIDEL)
                   SCL(1000,0,10,-10)
                   PLO(T,RMS1)
                   SCL(1000,0,5,0)
                   END
182.63                      POLAR GIMBAL SIMULATION
0          0
```

```
1.5          .376          .404          6.25E-3
.01          1             13            .05
1            0
$       ENDJOB
```

```
$       IDENT   366,54790,1087D,78294,ROY
$       LIMITS  65,30K,,10K,,1
$       PROGRAM RLHS,NDUMP
$       LIMITS  65,30000,,10000
$       PERM    M*,NIMIC-SYSTEM
$       TAPE    09,A23
A STELLAR TRACKING ATTITUDE REFERENCE SYSTEM     --- STARS ---
BEGIN DATA INPUT
ORBIT CONSTANTS
RO          DISTANCE FROM VEHICLE TO EARTH                  MILES
VO          MAGNITUDE OF EARTHS VELOCITY ABOUT SUN          MILES/SEC
(TO NEGLECT STELLAR ABERRATION SET RO=VO=0)
GAMMA       ORBIT INCLINATION ANGLE                         DEGREES
                  CON(RO,VO,GAMMA)
GIMBAL CONSTANTS
K1          PITCH DRIVER GAIN                               VOLTS/VOLT
KM1         PITCH MOTOR GAIN                                FT-LB/AMPS
KI1         PITCH INDUCTOSYN GAIN                           BITS/ARCSEC
KD1         PITCH D/A CONVERSION GAIN                       VOLTS/BIT
KF1         COULOMB FRICTION(PITCH AXIS)                    FT-LBS
TAU1        PITCH TIME CONSTANT 1                           SECONDS
TAU11       PITCH TIME CONSTANT 2                           SECONDS
R1          PITCH WINDING RESISTANCE                        OHMS
J1          PITCH INERTIA                                   SLUG-FT*FT
                  CON(K1,KM1,KI1,KD1,KF1)
                  CON(TAU1,TAU11,R1,J1)
K2          POLAR DRIVER GAIN                               VOLTS/VOLT
KM2         POLAR MOTOR                                     FT-LB/AMPS
KI2         POLAR INDUCTOSYN                                BITS/ARCSEC
KD2         POLAR D/A CONVERSION                            VOLTS/BIT
KF2         ELASTIC FRICTION COEFFICIENT(POLAR AXIS)        FT-LBS/ARCSEC
TAU2        POLAR TIME CONSTANT  1                          SECONDS
TAU12       POLAR TIME CONSTANT  2                          SECONDS
R2          POLAR WINDING RESISTANCE                        OHMS
J2          POLAR AXIS INERTIA                              SLUG-FT*FT
                  CON(K2,KM2,KI2,KD2,KF2)
                  CON(TAU2,TAU12,R2,J2)
BIAS ERROR COMPENSATION CONSTANTS
DELTHE      PITCH GIMBAL BIAS ERROR                         DEGREES
DELPHI      POLAR GIMBAL BIAS ERROR                         DEGREES
DELGAM      ORBIT INCLINATION BIAS ERROR                    DEGREES
BXJ         ROLL(TELESCOPE)BIAS FOR J-STAR                  DEGREES
BXK         ROLL(TELESCOPE)BIAS FOR K-STAR                  DEGREES
BYJ         YAW(TELESCOPE)BIAS FOR J-STAR                   DEGREES
BYK         YAW(TELESCOPE)BIAS FOR K-STAR                   DEGREES
BZJ         PITCH(TELESCOPE)BIAS FOR J-STAR                 DEGREES
BZK         PITCH(TELESCOPE)BIAS FOR K-STAR                 DEGREES
                  CON(DELTHE,DELPHI,DELGAM)
                  CON(BXJ,BYJ,BZJ,BXK,BYK,BZK)
TIME TO ANGLE CONVERSION CONSTANTS
KR          SCAN CIRCLE RADIUS                              DEGREES
P           SCANNING PERIOD                                 SEC
NPRH        MISSED PLUS FALSE PULSE RATE                    PER HOUR
                  CON(KR,P,NPRH)
CONTROL SYSTEM CONSTANTS
K2Y         CONTROL SYSTEM GAIN -- YAW                      FT-LBS/RAD
K2R         CONTROL SYSTEM GAIN -- ROLL                     FT-LBS/RAD
K2P         CONTROL SYSTEM GAIN -- PITCH                    FT-LBS/RAD
```

```
TAU1Y       LEAD TIME CONSTANT -- YAW                          SECONDS
TAU1R       LEAD TIME CONSTANT -- ROLL                         SECONDS
TAU1P       LEAD TIME CONSTANT -- PITCH                        SECONDS
TAU2Y       LAG TIME CONSTANT -- YAW                           SECONDS
TAU2R       LAG TIME CONSTANT -- ROLL                          SECONDS
TAU2P       LAG TIME CONSTANT -- PITCH                         SECONDS
                  CON(K2Y,TAU1Y,TAU2Y,K2R,TAU1R,TAU2R)
                  CON(K2P,TAU1P,TAU2P)
SPACECRAFT DYNAMICS CONSTANTS
IR          SPACECRAFT ROLL INERTIA                            SLUG-FT*FT
IP          SPACECRAFT PITCH INERTIA                           SLUG-FT*FT
IY          SPACECRAFT YAW INERTIA                             SLUG-FT*FT
IRY         SPACECRAFT ROLL-YAW CROSS INERTIA                  SLUG-FT*FT
                  CON(IR,IP,IY,IRY)
INITIAL CONDITIONS
ALPHA0      ALPHA IC                                           DEGREES
BETA0       BETA IC                                            DEGREES
THETA0      PITCH GIMBAL INITIAL POSITION                      ARCSECS
THETD0      PITCH GIMBAL INITIAL RATE                          ARCSEC/SEC
PHI0        POLAR GIMBAL INITIAL POSITION                      ARCSECS
PHID0       POLAR GIMBAL INITIAL RATE                          ARCSEC/SEC
                  CON(ALPHA0,BETA0)
                  CON(THETD0,THETA0,PHID0,PHI0)
YAWDIC      YAWDOT IC                                          ARCSEC/SEC
ROLDIC      ROLLDOT IC                                         ARCSEC/SEC
PITDIC      PITCHDOT IC                                        ARCSEC/SEC
YAW0        YAW IC                                             ARCSEC
ROL0        ROL IC                                             ARCSEC
PIT0        PIT IC                                             ARCSEC
                  PAR(YAWDIC,ROLDIC,PITDIC,YAW0,ROL0,PIT0)
T0          SIMULATION INITIAL TIME                            SECONDS
TFIN        SIMULATION FINISH TIME                             SECONDS
N           STEP SIZE = 1/(2**N)
PRINT       PRINTING INTERVAL                                  SECONDS
                  PAR(T0,TFIN,N,PRINT)
STAR SELECTION
DELTAJ      DECLINATION OF J-STAR                              DEGREES
DELTAK      DECLINATION OF K-STAR                              DEGREES
LAMDAJ      RIGHT ASCENSION OF J-STAR                          DEGREES
LAMDAK      RIGHT ASCENSION OF K-STAR                          DEGREES
                  PAR(DELTAJ,LAMDAJ,DELTAK,LAMDAK)
ETAK        RIGHT ASCENSION OF K-TELESCOPE BORESIGHT           DEGREES
ZETAK       DECLINATION OF K-TELESCOPE BORESIGHT               DEGREES
ETAJ        RIGHT ASCENSION OF J-TELESCOPE BORESIGHT           DEGREES
ZETAJ       DECLINATION OF J-TELESCOPE BORESIGHT               DEGREES
                  PAR(ZETAJ,ETAJ,ZETAK,ETAK)
PRELIMINARY CALCULATIONS
                  DBM(TRUE)
            SW1   FSW(T,FALSE,TRUE,FALSE)
 SW1        PIE   3.14159
 SW1        RTD   180/PIE
 SW1        C     186000
 SW1        KRDA  3600*RTD
 SW1        KA    KR*KRDA
 SW1        KP    (KD1*K1*KM1)/R1
 SW1        KS    (KD2*K2*KM2)/R2
 SW1        OMEG  (13.737*360)/(24*3600)
 SW1        OMEGA 360/(365.26*24*3600)
```

```
 SW1      ALPHAD    OMEG*3600
 SW1      BETAD     OMEGA*3600
 SW1      ALPHAB    OMEG
 SW1      SOMEGA    SIN(OMEGA*TI/RTD)
 SW1      COMEGA    COS(OMEGA*TI/RTD)
 SW1      COSE      COS(23.5/RTD)
 SW1      PSI       GAMMA
 SW1      CPSI      COS(PSI/RTD)
 SW1      SPSI      SIN(PSI/RTD)
 SW1      CGAMMA    COS(GAMMA/RTD)
 SW1      SGAMMA    SIN(GAMMA/RTD)
 SW1      CDELTJ    COS(DELTAJ/RTD)
 SW1      SDELTJ    SIN(DELTAJ/RTD)
 SW1      CDELTK    COS(DELTAK/RTD)
 SW1      SDELTK    SIN(DELTAK/RTD)
 SW1      CLAMDJ    COS(LAMDAJ/RTD)
 SW1      SLAMDJ    SIN(LAMDAJ/RTD)
 SW1      CLAMDK    COS(LAMDAK/RTD)
 SW1      SLAMDK    SIN(LAMDAK/RTD)
 SW1      CZETAK    COS(ZETAK/RTD)
 SW1      SZETAK    SIN(ZETAK/RTD)
 SW1      CZETAJ    COS(ZETAJ/RTD)
 SW1      SZETAJ    SIN(ZETAJ/RTD)
 SW1      CETAK     COS(ETAK/RTD)
 SW1      SETAK     SIN(ETAK/RTD)
 SW1      CETAJ     COS(ETAJ/RTD)
 SW1      SETAJ     SIN(ETAJ/RTD)
 SW1      I1        IY/KRDA
 SW1      I2        IR/KRDA
 SW1      I3        IP/KRDA
 SW1      I12       IRY/KRDA
RUN CONTROL LOGIC
 SW1      DTMIN     1/(2**N)
 SW1      DTMAX     DTMIN
 SW1      DT        1
          TI        T+T0
                    FIN(TI,TFIN)
MEMORY,TIMING,AND CONTROL
          SW2       FSW(REM(TI,.25),FALSE,TRUE,FALSE)
          SW3       FSW(REM(TI,90),FALSE,TRUE,FALSE)
          CALPHA    COS(ALPHA/RTD)
          SALPHA    SIN(ALPHA/RTD)
          ALPHA     OMEG*TI+ALPHA0
 SW3      BETA      OMEGA*TI+BETA0
 SW3      CBETA     COS(BETA/RTD)
 SW3      SBETA     SIN(BETA/RTD)
GIMBAL ANGLE COMMAND GENERATOR
          THECOM    (ALPHA+DELTHE)*3600
          STHETA    SIN(THETA/RTD)
          CTHETA    COS(THETA/RTD)
 SW3      PHICOM    (BETA+DELPHI)*3600
 SW3      SPHI      SIN(PHI/RTD)
 SW3      CPHI      COS(PHI/RTD)
PITCH GIMBAL EQUATIONS
          INDTEP    RNG(0,1.75,.1)
          BEAREP    RNG(0,1.137,.2)
 SW4      THETAC    ING(K11*THECOM)
          EI10      THETAC-THETA
```

```
          EI1       KP*EI10
          P21       INT(EI1,0)
          P11       INT((10*TAU1+TAU11)*EI1-EO1+P21,0)
          EO1       (10*TAU1*TAU11*EI1+P11)/TAU1
          OI1       (EO1+F1)/J1
          F1        FSW(THETAD,KF1,0,-KF1)
          THETAD    INT(OI1,THETD0)
          THETA     INT(THETAD,THETA0)
          THETAA    KRDA*THETA+BEAREP
          THETB     ING(KI1*(THETAA+INDTEP))
POLAR GIMBAL EQUATIONS
** ELASTIC FRICTION MODEL
 SW3      CO        PHI
          SW5       FSW(ABS(PHID)-.000001,FALSE,TRUE,FALSE)
          SW6       COM(SW5)
 SW5      F2        0
 SW6      C1        PHI-CO
 SW6      F2        -KF2*C1
****
          BEARER    RNG(0,1.137,.5)
          INDTER    RNG(0,1.75,.7)
 SW3      PHIC      ING(KI2*PHICOM)
          EI20      PHIC-PHB
          EI2       KS*EI20
          P22       INT(EI2,0)
          P12       INT((10*TAU2+TAU12)*EI2-EO2+P22,0)
          EO2       (10*TAU2*TAU12*EI2+P12)/TAU2
          OI2       (EO2+F2)/J2
          PHID      INT(OI2,PHID0)
          PHI       INT(PHID,PHI0)
          PHA       KRDA*PHI+BEARER
          PHB       ING(KI2*(PHA+INDTER))
OPTICAL STAR SENSORS
 SW2      AB11      CTHETA*CPHI-STHETA*CPSI*SPHI
 SW2      AB12      -STHETA*CPHI-CTHETA*CPSI*SPHI
 SW2      AB13      SPHI*SPSI
 SW2      AB21      CTHETA*SPHI+STHETA*CPSI*CPHI
 SW2      AB22      -STHETA*SPHI+CTHETA*CPSI*CPHI
 SW2      AB23      -SPSI*CPHI
 SW2      AB31      STHETA*SPSI
 SW2      AB32      CTHETA*SPSI
 SW2      AB33      CPSI
 SW2      EBX       YAW+PIR*ROL-ROR*PIT
 SW2      EBY       -PIR*YAW+ROL+YAR*PIT
 SW2      EBZ       ROR*YAW-YAR*ROL+PIT
 SW2      RX        AB11*EBX+AB12*EBY+AB13*EBZ
 SW2      RY        AB21*EBX+AB22*EBY+AB23*EBZ
 SW2      RZ        AB31*EBX+AB32*EBY+AB33*EBZ
 SW2      RHHXJ1    SZETAJ*CETAJ*RX+SZETAJ*SETAJ*RY-C   AJ*RZ
 SW2      RHHYJ1    -SETAJ*RX+CETAJ*RY
 SW2      RHHXK1    SZETAK*CETAK*RX+SZETAK*SETAK*RY-CZETAK*RZ
 SW2      RHHYK1    -SETAK*RX+CETAK*RY
 SW2      RHHXJ     LIM(RHHXJ1,-1800,1800)
 SW2      RHHYJ     LIM(RHHYJ1,-1800,1800)
 SW2      RHHXK     LIM(RHHXK1,-1800,1800)
 SW2      RHHYK     LIM(RHHYK1,-1800,1800)
PULSE INTERVAL TIMING
 SW2      TXJ       -P*ASN(RHHXJ/KA)/(2*PIE)
```

```
 SW2      TYJ      P*ASN(RHHYJ/KA)/(2*PIE)
 SW2      TXK      -P*ASN(RHHXK/KA)/(2*PIE)
 SW2      TYK      P*ASN(RHHYK/KA)/(2*PIE)
TIME TO ANGLE CONVERSION
 SW1      MPN      ING(MPRH*(TFIN-T0)/3600)
 SW2      MP1      ING((TFIN-T0)*RNU(0,1,1)/P)
 SW2      MP2      ING((TFIN-T0)*RNU(0,1,2)/P)
 SW2      MP3      ING((TFIN-T0)*RNU(0,1,3)/P)
 SW2      MP4      ING((TFIN-T0)*RNU(0,1,4)/P)
 SW2      YES1     FSW(MP1-MPN,TRUE,TRUE,FALSE)
 SW2      YES2     FSW(MP2-MPN,TRUE,TRUE,FALSE)
 SW2      YES3     FSW(MP3-MPN,TRUE,TRUE,FALSE)
 SW2      YES4     FSW(MP4-MPN,TRUE,TRUE,FALSE)
 SW2      NO1      COM(YES1)
 SW2      NO2      COM(YES2)
 SW2      NO3      COM(YES3)
 SW2      NO4      COM(YES4)
 SW2      JITXJ    RNG(0,1.15,2)
 SW2      JITYJ    RNG(0,1.15,3)
 SW2      JITXK    RNG(0,1.15,4)
 SW2      JITYK    RNG(0,1.15,5)
 NO1      RHOXJ    KA*SIN(-2*PIE*TXJ/P)+JITXJ
 NO1      FP1      0.0
 NO2      RHOYJ    KA*SIN(2*PIE*TYJ/P)+JITYJ
 NO2      FP2      0.0
 NO3      RHOXK    KA*SIN(-2*PIE*TXK/P)+JITXK
 NO3      FP3      0.0
 NO4      RHOYK    KA*SIN(2*PIE*TYK/P)+JITYK
 NO4      FP4      0.0
 YES1     RHOXJ    TDL(RHOXJ,DTMIN,75)
 YES1     FP1      1.0
 YES2     RHOYJ    TDL(RHOYJ,DTMIN,75)
 YES2     FP2      1.0
 YES3     RHOXK    TDL(RHOXK,DTMIN,75)
 YES3     FP3      1.0
 YES4     RHOYK    TDL(RHOYK,DTMIN,75)
 YES4     FP4      1.0
ORBIT PERTURBATIONS
 SW1      NUXJ     DELGAM*SDELTJ*CLAMDJ
 SW1      NUYJ     -DELGAM*SLAMDJ
 SW1      NUXK     DELGAM*SDELTK*CLAMDK
 SW1      NUYK     -DELGAM*SLAMDJ
STELLAR ABERRATION
 SW3      V11      -ALPHAB*SALPHA*(CBETA*CGAMMA-SBETA*SGAMMA)
 SW3      V1       V11-ALPHAB*CALPHA*(CBETA*SGAMMA+SBETA*CGAMMA)
 SW3      V21      -ALPHAB*SALPHA*(SBETA*CGAMMA+CBETA*SGAMMA)
 SW3      V2       V21-ALPHAB*CALPHA*(SBETA*SGAMMA-CBETA*CGAMMA)
 SW3      AXJ      (VO*COSE*SOMEGA+RO*(-SLAMDJ*V1+CLAMDJ*V2))/C
 SW3      AXK      (VO*COSE*SOMEGA+RO*(-SLAMDK*V1+CLAMDK*V2))/C
 SW3      AYJ      -(VO*COMEGA+RO*(SDELTJ*CLAMDJ*V1+SDELTJ*SLAMDJ*V2))/C
 SW3      AYK      -(VO*COMEGA+RO*(SDELTK*CLAMDK*V1+SDELTK*SLAMDK*V2))/C
TELESCOPE BIASES
 SW1      XIXJ     SZETAJ*CETAJ*BXJ+SZETAJ*SETAJ*BYJ-CZETAJ*BZJ
 SW1      XIYJ     -SETAJ*BXJ+CETAJ*BYJ
 SW1      XIXK     SZETAK*CETAK*BXK+SZETAK*SETAK*BYK-CZETAK*BZK
 SW1      XIYK     -SETAK*BXK+CETAK*BYK
BIAS COMPENSATION
 SW2      MUXJ     RHOXJ+(XIXJ+NUXJ+AXJ)*3600
```

```
SW2     MUXK    RHOXK+(XIXK+NUXK+AXK)*3600
SW2     MUYJ    RHOYJ+(XIYJ+NUYJ+AYJ)*3600
SW2     MUYK    RHOYK+(XIYK+NUYK+AYK)*3600
COORDINATE TRANSFORMATION AND ERROR ESTIMATION
SW2     R11     CALPHA*CBETA-SALPHA*SBETA*CGAMMA
SW2     R12     -SALPHA*CBETA-CALPHA*SBETA*CGAMMA
SW2     R13     SBETA*SGAMMA
SW2     R21     CALPHA*SBETA+SALPHA*CBETA*CGAMMA
SW2     R22     -SALPHA*SBETA+CALPHA*CBETA*CGAMMA
SW2     R23     -SGAMMA*CBETA
SW2     R31     SALPHA*SGAMMA
SW2     R32     CALPHA*SGAMMA
SW2     R33     CGAMMA
SW2     R11J    SDELTJ*CLAMDJ*R11+SDELTJ*SLAMDJ*R21-CDELTJ*R31
SW2     R12J    SDELTJ*CLAMDJ*R12+SDELTJ*SLAMDJ*R22-CDELTJ*R32
SW2     R13J    SDELTJ*CLAMDJ*R13+SDELTJ*SLAMDJ*R23-CDELTJ*R33
SW2     R21J    -SLAMDJ*R11+CLAMDJ*R21
SW2     R22J    -SLAMDJ*R12+CLAMDJ*R22
SW2     R23J    -SLAMDJ*R13+CLAMDJ*R23
SW2     R11K    SDELTK*CLAMDK*R11+SDELTK*SLAMDK*R21-CDELTK*R31
SW2     R12K    SDELTK*CLAMDK*R12+SDELTK*SLAMDK*R22-CDELTK*R32
SW2     R13K    SDELTK*CLAMDK*R13+SDELTK*SLAMDK*R23-CDELTK*R33
SW2     R21K    -SLAMDK*R11+CLAMDK*R21
SW2     R22K    -SLAMDK*R12+CLAMDK*R22
SW2     R23K    -SLAMDK*R13+CLAMDK*R23
SW2     A11     R11J*R11J+R21J*R21J+R11K*R11K+R21K*R21K
SW2     A12     R11J*R12J+R21J*R22J+R11K*R12K+R21K*R22K
SW2     A13     R11J*R13J+R21J*R23J+R11K*R13K+R21K*R23K
SW2     A21     A12
SW2     A22     R12J*R12J+R22J*R22J+R12K*R12K+R22K*R22K
SW2     A23     R12J*R13J+R22J*R23J+R12K*R13K+R22K*R23K
SW2     A31     A13
SW2     A32     A23
SW2     A33     R13J*R13J+R23J*R23J+R13K*R13K+R23K*R23K
SW2     DETA1   A11*(A22*A33-A23*A32)+A12*(A23*A31-A21*A33)
SW2     DETA    DETA1+A13*(A21*A32-A22*A31)
SW2     A11IN   (A22*A33-A23*A32)/DETA
SW2     A12IN   (A13*A32-A12*A33)/DETA
SW2     A13IN   (A12*A23-A13*A22)/DETA
SW2     A21IN   (A23*A31-A21*A33)/DETA
SW2     A22IN   (A11*A33-A13*A31)/DETA
SW2     A23IN   (A13*A21-A11*A23)/DETA
SW2     A31IN   (A21*A32-A22*A31)/DETA
SW2     A32IN   (A12*A31-A11*A32)/DETA
SW2     A33IN   (A11*A22-A12*A21)/DETA
SW2     AS11    A11IN*R11J+A12IN*R12J+A13IN*R13J
SW2     AS12    A11IN*R21J+A12IN*R22J+A13IN*R23J
SW2     AS13    A11IN*R11K+A12IN*R12K+A13IN*R13K
SW2     AS14    A11IN*R21K+A12IN*R22K+A13IN*R23K
SW2     AS21    A21IN*R11J+A22IN*R12J+A23IN*R13J
SW2     AS22    A21IN*R21J+A22IN*R22J+A23IN*R23J
SW2     AS23    A21IN*R11K+A22IN*R12K+A23IN*R13K
SW2     AS24    A21IN*R21K+A22IN*R22K+A23IN*R23K
SW2     AS31    A31IN*R11J+A32IN*R12J+A33IN*R13J
SW2     AS32    A31IN*R21J+A32IN*R22J+A33IN*R23J
SW2     AS33    A31IN*R11K+A32IN*R12K+A33IN*R13K
SW2     AS34    A31IN*R21K+A32IN*R22K+A33IN*R23K
SW2     EAX1    AS11*MUXJ+AS12*MUYJ+AS13*MUXK+AS14*MUYK
```

```
 SW2      EAY1      AS21*MUXJ+AS22*MUYJ+AS23*MUXK+AS24*MUYK
 SW2      EAZ1      AS31*MUXJ+AS32*MUYJ+AS33*MUXK+AS34*MUYK
CONTROL SYSTEM DEADBAND
          ON1       FSW(ABS(EAX1)-1.,FALSE,TRUE,TRUE)
          ON2       FSW(ABS(EAY1)-1.,FALSE,TRUE,TRUE)
          ON3       FSW(ABS(EAZ1)-1.,FALSE,TRUE,TRUE)
          OFF1      COM(ON1)
          OFF2      COM(ON2)
          OFF3      COM(ON3)
 ON1      EAX       EAX1
 ON2      EAY       EAY1
 ON3      EAZ       EAZ1
 OFF1     EAX       0
 OFF2     EAY       0
 OFF3     EAZ       0
 SW2      ERX       -EAX/KRDA
 SW2      ERY       -EAY/KRDA
 SW2      ERZ       -EAZ/KRDA
CONTROL SYSTEM
          AC2Y      INT(2*K2Y*TAU1Y*ERX-TY+INT(K2Y*ERX,0),0)
          AC2R      INT(2*K2R*TAU1R*ERY-TR+INT(K2R*ERY,0),0)
          AC2P      INT(2*K2P*TAU1P*ERZ-TP+INT(K2P*ERZ,0),0)
          TY        (K2Y*TAU1Y*TAU1Y*ERX+AC2Y)/TAU2Y
          TR        (K2R*TAU1R*TAU1R*ERY+AC2R)/TAU2R
          TP        (K2P*TAU1P*TAU1P*ERZ+AC2P)/TAU2P
DISTURBANCE TORQUES --GRAVITY GRADIENT+SOLAR PRESSURE
          TGR       -3.0*(OMEG/RTD)*(OMEG/RTD)*(IP-IY)*SIN(2.0*ROR)
          TGP       -3.0*(OMEG/RTD)*(OMEG/RTD)*(IR-IP)*SIN(2.0*PIR)
          TGY       0.0
          TSR       .00001*COS(OMEG*TI/RTD)
          TSY       .00001*SIN(OMEG*TI/RTD)
          TSP       0.0
          TXDIS     TGY+TSY
          TYDIS     TGR+TSP
          TZDIS     TGP+TSP
SPACECRAFT DYNAMICS ---EOS---
          DTY       ((I3-I2)*WPIT*WROL-I12*WYAW*WPIT)/KRDA
          DTR       ((I1-I3)*WYAW*WPIT+I12*WROL*WPIT)/KRDA
          DTP       ((I2-I1)*WYAW*WROL+I12*(WYAW*WYAW-WROL*WROL))/KRDA
          T1        TY-DTY+TYDIS
          T2        TR-DTR+TYDIS
          T3        TP-DTP+TZDIS
          DET       I1*I2-I12*I12
          WXD       (I2*T1-I12*T2)/DET
          WYD       (I1*T2-I12*T1)/DET
          WZD       T3/I3
 SW1      YAWD0     WXORB+YAWDIC
 SW1      ROLD0     WYORB+ROLDIC
 SW1      PITD0     WZORB+PITDIC
          WYAW      INT(WXD,YAWD0)
          WROL      INT(WYD,ROLD0)
          WPIT      INT(WZD,PITD0)
          WXORB     R31*OMEGA*3600
          WYORB     R32*OMEGA*3600
          WZORB     R33*OMEGA*3600+OMEG*3600
          WXR       WXORB+PIR*WYORB-ROR*WZORB
          WYR       -PIR*WXORB+WYORB+YAR*WZORB
          WZR       ROR*WZORB-YAR*WYORB+WZORB
```

```
          WYBR      (WYAW-WXR)+YAR*ROR*(WROL-WYR)+ROR*(WPIT-WZR)
          WRBR      (WROL-WYR)-(WPIT-WZR)*YAR
          WPBR      (WROL-WYR)*YAR+(WPIT-WZR)
          YAW       INT(WYBR,YAW0)
          ROL       INT(WRBR,ROL0)
          PIT       INT(WPBR,PIT0)
          PIR       PIT/KRDA
          ROR       ROL/KRDA
          YAR       YAW/KRDA
          H1        I1*WYAW+I12*WROL
          H2        I2*WROL+I12*WYAW
          H3        I3*WPIT
          H         SQR(H1*H1+H2*H2+H3*H3)
OUTPUT DISPLAY
          THEDEL    THECOM-THETAA
          PHIDEL    PHICOM-PHA
          R         (1/T)*INT(THEDEL,0)
          RMS       SQR(ABS((1/T)*INT(THEDEL*THEDEL,0)-R*R))
          R1        (1/T)*INT(PHIDEL,0)
          RMS1      SQR(ABS((1/T)*INT(PHIDEL*PHIDEL,0)-R1*R1))
          ERSTRX    YAW-EAX
          ERSTRY    ROL-EAY
          ERSTRZ    PIT-EAZ
          OUTP      FSW(REM(TI,PRINT),FALSE,TRUE,FALSE)
 OUTP               OUT
 OUTP               OUT
 OUTP               OUT(TI)
 OUTP               OUT(THETA,ALPHA,THETAA,THECOM,THEDEL,RMS)
 OUTP               OUT(PHI,BETA,PHA,PHICOM,PHIDEL,RMS1)
 OUTP               OUT(RHHXJ1,RHHYJ1,RHHXK1,RHHYK1)
 OUTP               OUT(RHHXJ,RHHYJ,RHHXK,RHHYK)
 OUTP               OUT(TXJ,TYJ,TXK,TYK)
 OUTP               OUT(FP1,FP2,FP3,FP4)
 OUTP               OUT(MP1,MP2,MP3,MP4,MPN)
 OUTP               OUT(JITXJ,JITYJ,JITXK,JITYK)
 OUTP               OUT(RHOXJ,RHOYJ,RHOXK,RHOYK)
 OUTP               OUT(EAX,EAY,EAZ,TY,TR,TP)
 OUTP               OUT(ERSTRX,ERSTRY,ERSTRZ)
 OUTP               OUT(TY,TR,TP,T1,T2,T3)
 OUTP               OUT(WYBR,WRBR,WPBR)
 OUTP               OUT(WYAW,WROL,WPIT,YAW,ROL,PIT)
                    PLO(TI,EAX,EAY,EAZ)
                    SCL(TFIN,T0,5,-5)
                    PLO(TI,WYAW,WROL)
                    SCL(TFIN,T0,.10,-.10)
                    PLO(TI,WPIT)
                    SCL(TFIN,T0,210,200)
                    PLO(TI,YAW,ROL,PIT)
                    SCL(TFIN,T0,5,-5)
                    END
0           0           99
200         .376        .404        6.25E-3     .026
.01         1           13          1.5
.8          .376        .404        6.25E-3     182.63
.01         1.0         13          .05
0           0           0
0           0           0           0           0           0
1           .25         140
```

```
.01          67          6.7          .01          67          6.7
.01          67          6.7
500          1000        1000         0
0            0           0            0            0           0
0            0           0            0
0            0           0            0            0           0
0            3000        4            50
-8.24        78.25       -56.84       305.78
-8.24        78.25       -56.84       305.78
$       ENDJOB
```